PHYSICAL REVIEW FLUIDS **2**, 103302 (2017)

Growth of viscoelastic wings and the reduction of particle mobility in a viscoelastic shear flow

William L. Murch,[1,*] Sreenath Krishnan,[2] Eric S. G. Shaqfeh,[1,2,3,†] and Gianluca Iaccarino[2,3]
[1]*Department of Chemical Engineering, Stanford University, Stanford, California 94305, USA*
[2]*Department of Mechanical Engineering, Stanford University, Stanford, California 94305, USA*
[3]*Institute for Computational and Mathematical Engineering, Stanford University, Stanford, California 94305, USA*

(Received 29 January 2017; revised manuscript received 15 July 2017; published 25 October 2017)

The motion of a rigid spherical particle in a sheared polymeric fluid is studied via experiments and numerical simulations. We study particle mobility in highly elastic fluids, where the deformation due to the sphere's movement and the shear flow both result in significant stretching of the polymer. The shear flow is imposed in a plane perpendicular to the sphere's movement, resulting in regions of high polymer tension in the wake of the sphere that can extend well into the shear flow and gradient directions. We observe that these viscoelastic wake structures, resembling wings, are linked to an increase in the form drag, providing a mechanism for a dramatic decrease in the particle mobility.

DOI: 10.1103/PhysRevFluids.2.103302

I. INTRODUCTION

Particle mobility is a critical factor in physical processes involving the transport of suspended particles. Particles suspended in liquids are ubiquitous in engineered processes, biological systems, and natural settings. Engineering examples can be found in oilfield applications, separations, microfluidics, and three-dimensional (3D) printing. In these applications, it is crucial to control and predict the mobility of the particles. Often, this task is complicated by the complex nature of the fluid phase, which may exhibit a nonlinear relationship between the fluid stress and an applied strain rate. This non-Newtonian behavior is often a result of fluid viscoelasticity, in which the fluid response to a deformation includes both viscous and elastic contributions. Viscoelasticity is observed across a wide range of fluids and applications [1]. In some cases, these fluids are designed with viscoelasticity specifically to control the movement of a dispersed particle phase [2,3].

For a rigid, spherical particle moving in the limit of a vanishingly small Reynolds number Re in an infinite Newtonian fluid, the particle mobility, M_{ij}, i.e., the tensor of proportionality between applied force and particle velocity, $U_i = M_{ij} F_j$, is given by the well known Stokes law, $F_i = 6\pi\eta a U_i$, where F_i is the applied force, η is the fluid viscosity, a is the sphere radius, and U_i is the steady particle velocity [4]. When fluid inertia is negligible in Newtonian fluids, the governing equations of motion become linear and thus linear superpositions of simple solutions are also solutions of the Stokes equations. Thus, for a settling sphere, a simple shear flow imposed in a direction perpendicular to gravity, termed orthogonal shear (or cross shear), will not affect the particle mobility in the gravitational direction and the settling rate will remain unchanged, although the particle will rotate about the axis aligned with gravity. However, even at vanishing inertia, fluid viscoelasticity breaks the linearity (and reversibility) of the Stokes solution. In this paper, we address why and how the mobility of such a particle changes in a viscoelastic fluid with an imposed orthogonal shear flow.

As is well known, viscoelasticity is a characteristic commonly found in polymeric solutions and melts [5,6]. Polymers in solution favor a coiled isotropic structure due to constant thermally

---

[*] murch@stanford.edu
[†] esgs@stanford.edu

driven bombardment, for example, by solvent molecules. A mechanical deformation of a polymeric fluid stretches the polymer molecules anisotropically while entropic forces act to bring the polymer back to its preferred coiled state, imparting elasticity to the fluid. The restoring force or tension on the polymer molecule results in an extra stress in the fluid and the relaxation mechanism of the polymer molecule introduces a characteristic polymer relaxation time scale. In addition to elasticity, polymeric fluids often exhibit a shear thinning viscosity. To decouple the often competing effects of elasticity and shear thinning, we use model elastic (or Boger) fluids in our study [7].

The sedimentation of spherical particles in viscoelastic fluids without shear has been studied extensively [8–10]. A dimensionless Weissenberg number, which relates the polymer relaxation time scale to the flow time scale, can be defined as the product of the relaxation time λ and a characteristic deformation rate, e.g., $U/2a$, where $U = |U_i|$. It has been shown that the mobility of the particle depends on this sedimentation Weissenberg number, defined here as $\Theta = U\lambda/2a$. Interestingly, for model elastic fluids, the functional dependence can change based on the regime of sedimentation Weissenberg number [10]. For sedimentation Weissenberg numbers larger than unity, the deformation of a polymer is dominated by the flow caused by the motion of the sphere and significant extension of the polymer can occur. It is therefore in this regime that elastic effects in the wake of the sphere become most pronounced, often resulting in enhanced drag [11–13]. The effect of viscoelasticity on a sphere's rotation in a simple shear flow has also been studied with experiments [14], theory [15], and numerical simulations [16,17]. These results exhibit good agreement, showing a reduction in the sphere's rotation rate relative to the Newtonian result.

This paper will also investigate the effect of particle confinement on the mobility, or, inversely, on the drag, experienced by the particle. In practical applications, especially with shearing flows, often the particle is confined by walls. The effect of particle confinement on particle mobility has been studied in Newtonian fluids, with the earliest theoretical work performed by Faxén [18], who used the method of reflections and showed a decrease in mobility due to confinement. A number of authors since have performed similar calculations of the drag enhancement on a particle moving parallel to confining walls [19–21]. An experimental study was later performed [22], producing an empirical prediction for the wall-corrected drag on a particle translating between two parallel walls in a viscous fluid. Studies of the effect of particle confinement on the drag in a viscoelastic fluid are more limited, particularly for a particle moving parallel to confining walls [10].

The study of particles settling in a viscoelastic fluid under an imposed orthogonal shear flow involves the combination of two canonical flow fields: uniform flow past the sphere and an orthogonal simple shear flow. This type of flow was first examined experimentally and it was observed that the particle settling rate may be significantly reduced in elastic fluids [23]. A theoretical basis for this result was not proposed until 20 years later, when a perturbation expansion for weakly elastic fluids showed decreased mobility for particles moving in orthogonal shear [24–26]. A simplified model force balance was presented for weakly elastic fluids [27], proposing that elastic tension acting along the streamlines, deformed by the particle sedimentation, was responsible for the enhanced drag. Later, a perturbation theory addressed the effect of the orientation of forcing relative to the shear flow on the particle mobility [28]. Further experiments showed that a shear-thinning viscosity and fluid elasticity can have opposing effects on the settling rate of particles under orthogonal shear [29–31]. Thereafter, numerical simulations of this phenomenon were performed and compared to the experiments and theory [32] and subsequently the effects of confinement and shear thinning were examined [33]. To summarize then, both numerical simulations [32] and a perturbation theory [27] have been used to propose mechanisms for the decrease in particle mobility in weakly elastic fluids. In this context, we define weakly elastic as meaning that the motion associated with the applied force (e.g., gravity) alone creates a very small deformation of the polymers in the fluid and thus the polymer deformation is dominated by the shear flow. In dimensionless terms, the sedimentation Weissenberg number Θ is small while the shear Weissenberg number $\mathrm{Wi} = \dot{\gamma}\lambda$, where $\dot{\gamma}$ is the shear rate, is finite. All previous studies of particle mobility in orthogonal shear have considered this range of parameters. However, in this paper, we consider the mobility of a rigid spherical particle moving under vanishing inertial forces in a highly elastic fluid, i.e., one in which the sedimentation

Weissenberg number is not small, under orthogonal shear. The regime where the sedimentation Weissenberg number is $O(1)$ is notably less explored and yet it is important for a number of reasons. First, this parameter regime is relevant to any application where a particle moves an $O(1)$ particle diameter per polymer relaxation time, achievable, for example, in oilfield applications or industrial separation processes. Second, as discussed above, the motion of the sphere in this parameter regime can result in significant extension of the polymer and elastic effects in the wake of the sphere become most pronounced. We show that in a highly elastic fluid (as defined above), there is an even more pronounced decrease in the particle mobility at increasing orthogonal shear rates. This reduction in particle mobility is directly related to the formation of winglike wake structures of high polymer tension that form around the particle when subjected to this fully 3D flow. We propose a mechanism for why these viscoelastic wings form and how their structure affects the mobility of the particle.

The paper is organized as follows. In Sec. II, the problem is defined, including the governing equations of motion and the boundary conditions, and the numerical scheme for simulations is outlined. In Sec. III, the experimental setup is described, including the fluid rheology and the experimental apparatus. In Sec. IV, the results of the experiments and numerical simulations are presented and the model for the coupling drag is explained. In Sec. V, the results are discussed and analyzed. A summary is given in Sec. VI.

II. PROBLEM FORMULATION

A. Problem definition

In this paper, we consider the sedimentation of a sphere in an orthogonal shear flow in a viscoelastic fluid. In our experiments, a shear flow in the plane perpendicular to gravity is imposed while a dense sphere is released in the fluid and allowed to settle, reaching a steady-state (terminal) velocity. In our simulations, we solve the equivalent problem but in a reference frame translating with the sphere. The governing equations of motion for the polymeric fluid flow are described, including the choice of a constitutive model, in Sec. II B. We discuss the implementation and boundary conditions for our simulations, as well as the computational mesh used, in Sec. II C.

B. Equation of motion and dimensionless parameters

In order to model the results of these experiments, we need to develop conservation of momentum in the fluid surrounding a given particle, including the viscoelastic fluid stress. Thus, the governing flow equations in dimensionless form are

$$\frac{\partial u_i}{\partial x_i} = 0, \tag{1}$$

$$\frac{\partial u_i}{\partial t} + u_j \frac{\partial u_i}{\partial x_j} = -\frac{1}{\mathrm{Re}} \frac{\partial p}{\partial x_i} + \frac{\beta}{\mathrm{Re}} \frac{\partial^2 u_i}{\partial x_j \partial x_j} + \frac{1-\beta}{\mathrm{Re}} \frac{\alpha}{\mathrm{Wi}} \frac{\partial \sigma_{ij}^P}{\partial x_j} + f_i, \tag{2}$$

where u_i is the fluid velocity, p is pressure, β is the solvent contribution to viscosity, σ_{ij}^P is the stress due to the elasticity of the polymers, and f_i is the body force (gravity, for example). The shear Weissenberg number Wi is defined as $\mathrm{Wi} = \lambda\dot{\gamma}$, the product of the polymer relaxation time scale λ and the shear deformation rate $\dot{\gamma}$. The ratio of the shear and sedimentation Weissenberg numbers is given by $\alpha = \mathrm{Wi}/\Theta$. We define the sedimentation Weissenberg number as $\Theta = \lambda U_{\mathrm{sed}}/2a$, i.e., the product of the polymer relaxation time and a characteristic deformation rate due to sphere settling $U_{\mathrm{sed}}/2a$. The definition for the sedimentation Weissenberg number is the same as that used by Padhy *et al.* [32,33]. Other authors have used a similar dimensionless parameter, the Deborah number $\mathrm{De} = \lambda U_{\mathrm{sed}}/a$ [8,11–13,24]. As we show later, the value of Θ depends partially on Wi due to enhanced drag caused by the orthogonal shear flow; thus, we also define a sedimentation Weissenberg number in the absence of shear, i.e., $\Theta_0 = \Theta(\mathrm{Wi} = 0)$, which indirectly represents the forcing of the sphere. In order to close the system of equations, we use the finitely extensible nonlinear elastic constitutive model with Peterlin closure (the FENE-P model) to describe the polymer stress [5,6]:

$$\sigma_{ij}^{P} = \frac{c_{ij}}{1 - c_{kk}/L^2} - \delta_{ij}, \tag{3}$$

$$\frac{\partial c_{ij}}{\partial t} + u_k \frac{\partial c_{ij}}{\partial x_k} - c_{ik}\frac{\partial u_j}{\partial x_k} - c_{kj}\frac{\partial u_i}{\partial x_k} = -\frac{\alpha}{\mathrm{Wi}}\sigma_{ij}^{P}, \tag{4}$$

where c_{ij} is the dimensionless polymer conformation tensor and L is the dimensionless maximum polymer extensibility, with both quantities scaled appropriately by the equilibrium Hookean spring length. In the FENE-P model, an individual member of a dilute concentration of polymers is approximated as a single dumbbell connected with a finitely extensible nonlinear elastic spring. Although a simplified molecular description, the FENE-P model captures the essential qualitative behavior of polymer chains in steady motion, as the modeled elastic dumbbells are both orientable and stretchable up to a finite extension [5,6]. This makes the FENE-P model appropriate for describing fluids that exhibit elasticity with modest shear thinning. This constitutive model is also useful in scenarios with high rates of deformation, as the polymer stress remains bounded.

Although the FENE-P dumbbell model captures the essential qualitative behavior of polymer chains in steady motion, we do not expect this constitutive model to be able to quantitatively predict hydrodynamic quantities for polymeric fluids. As will be discussed in Sec. III A, a single-mode FENE-P model is fit to shear rheology data to obtain model parameters for our numerical simulations. Clearly, the sedimentation of a sphere under orthogonal shear contains local regions of shear-dominant and extensional-dominant flow. In the case of a sphere settling in a quiescent viscoelastic fluid, the extensional region in the wake of the sphere becomes particularly important at higher sedimentation Weissenberg number, as discussed in Sec. I. The extensional rheology of these polymeric fluids may be inadequately captured by fitting only to shear rheology data. Additionally, polymeric fluids will exhibit multiple modes of relaxation, the dynamics of which may be only approximated by fitting to a single relaxation mode. Further to the point, Yang and Khomami [34] performed a thorough analysis of molecular-based constitutive models, comparing simulation data to the experimental data [13] for a sphere settling in a cylindrical tube. They reached the conclusion that single-mode dumbbell models, even when fit to extensional rheology data, do not contain the underlying physics required to quantitatively predict the drag on a sphere, although qualitative prediction of trends is possible. In their study, even multimode models were inadequate for quantitative prediction. Later, it was shown that a multiscale approach [35] or the inclusion of dissipative stress contributions [36] is needed for better quantitative description of the drag. There is little reason to believe that the complex 3D flow studied here will be better captured than in the pure settling problem. In this work, we therefore aim to explain qualitatively the mechanism for drag increase in sheared viscoelastic fluids.

C. Numerical scheme and boundary conditions

The schematic of the simulation is shown in Fig. 1 with the boundary conditions. Simulations were performed in a frame of reference translating with the sphere. The simulation domain is of length $L_x = 20a$ along the sedimentation direction and $L_z = 60a$ along the periodic direction. The lengths are chosen such that the results are domain converged at the highest Wi and Θ. The domain mesh was a boundary-fitted mesh and did not move or stretch during the simulation; translation and rotation of the sphere were achieved through modification of the appropriate boundary conditions. The orthogonal shear flow was applied by enforcing a no-slip boundary condition at the upper and lower plates and moving them with equal velocity U_{shear} in the opposite directions. Periodic boundary conditions were applied in the shear flow direction. We solved the mobility problem, where the external force acting on the sphere (gravity) was specified and we solved for the settling velocity U_{sed} and the rotational velocity iteratively using the force and torque acting on the sphere, respectively. The sphere did not translate but was allowed to freely rotate through modification of

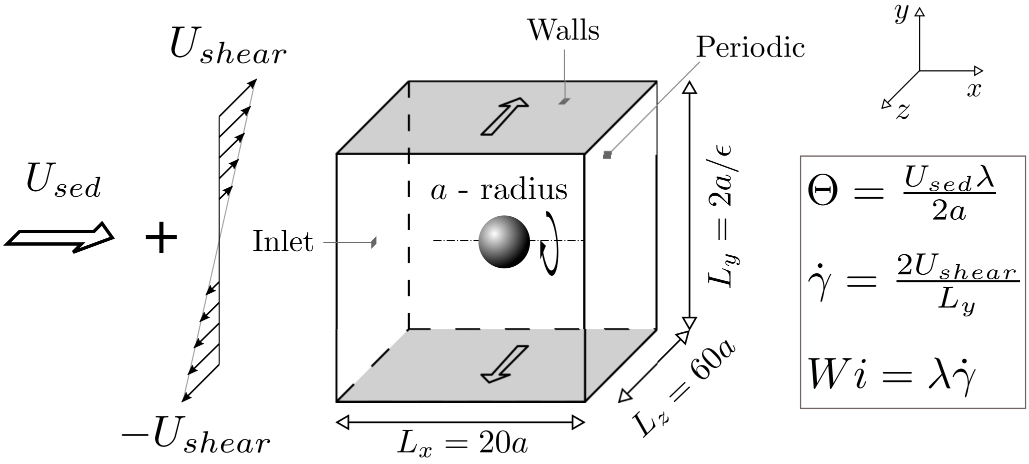

FIG. 1. Computational domain and boundary conditions used for the simulation.

the velocity boundary condition. At steady state, the hydrodynamic force balances the gravitational force and there is no net torque on the sphere. The velocity at the inlet is specified as a combination of the settling velocity and shear flow in orthogonal directions. The polymer conformation components at the inlet are specified using the analytical solution for a FENE-P fluid in a shear flow [37]. There is no need to specify boundary conditions for c_{ij} at the walls, since for control volumes on the boundary there is no flux through the faces coinciding with the walls and hence c_{ij} at the boundary is completely determined by fluxes through other faces in the control volume and source term contributions. A convective outlet boundary condition is used for both u_i and c_{ij} at the outflow boundary.

The calculations were accomplished using a massively parallel, three-dimensional code, based on an unstructured finite-volume formulation for the numerical calculations. The details of the solver, as well as extensive validation tests, can be found in prior studies by Richter *et al.* [38], Padhy *et al.* [32,33], and Yang *et al.* [39].

A tetrahedral discretization of the domain shown in Fig. 1 is used for the simulations. The mesh contains between 2.6×10^6 and 6.7×10^6 elements, with smaller elements near the surface of the sphere (of resolution $a/20$ to $a/40$) in order to resolve the stress gradients accurately. The results presented in this paper are converged in both domain size and the mesh resolution.

III. EXPERIMENTAL SETUP

A. Fluid rheology

Two fluids were used in this study, both of which were aqueous, polyacrylamide-based polymeric fluids. In order to isolate the effect of fluid elasticity, these fluids were designed to have a low concentration of a high-molecular-weight polymer in a viscous solvent, with the intent to have high fluid elasticity with a minimally shear thinning viscosity. This class of fluids is referred to as model elastic or Boger fluids [7,40,41], as mentioned in Sec. I. The two fluids utilized the same components, but with different viscosity solvents and different formulations. We will refer to the fluids as BF1 (Boger fluid 1) and BF2 (Boger fluid 2).

For BF1, the Newtonian solvent component was a 7:3 mass ratio mixture of a relatively-low-viscosity corn syrup (Fisher Scientific) to glycerol (Sigma-Aldrich, ⩾99%). The non-Newtonian polymer component was a 2 wt. % polyacrylamide (Sigma-Aldrich, $M_w \approx 5 \times 10^6$ g/mol) solution. The Newtonian solvent and polymer solution were mixed at a 10:1 mass ratio. In summary, the final concentration of each component was 63.64 wt. % corn syrup, 27.27 wt. % glycerol, 0.18 wt. %

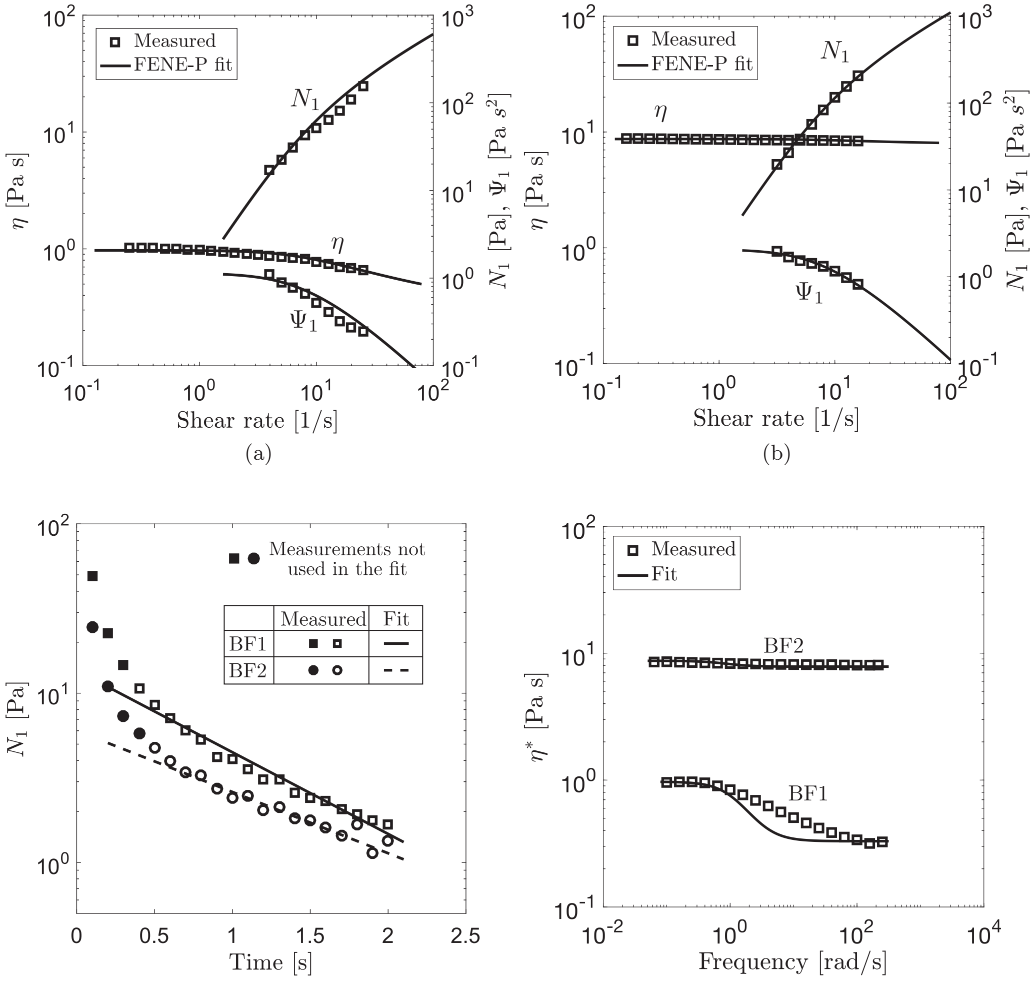

(a) (b) (c) (d)

FIG. 2. Rheological measurements for BF1 and BF2 (symbols) and the FENE-P model fits (lines) from (a) steady-shear BF1, (b) steady-shear BF2, (c) transient stress relaxation following a step strain (strain equal to 500%), and (d) small-amplitude oscillatory shear experiments.

polyacrylamide, and the balance deionized water. The density of the fluid was $\rho_f = 1302.6$ kg/m^3. For BF2, the Newtonian solvent component was a 7:3 mass ratio mixture of a relatively-high-viscosity corn syrup (Frey Scientific) to glycerol (Sigma-Aldrich, $\geqslant$99%). The non-Newtonian polymer (or solute) component was the same 2 wt. % polyacrylamide solution as for BF1. The Newtonian solvent and polymer solution were mixed at a 200:1 mass ratio. In summary, the final concentration of each component was 69.64 wt. % corn syrup, 29.85 wt. % glycerol, 0.010 wt. % polyacrylamide, and the balance deionized water. The density of the fluid was $\rho_f = 1357.8$ kg/m^3.

The fluid was characterized using a rotational rheometer (ARES-G2, TA Instruments) with a 25-mm-diam 0.1 rad cone-and-plate geometry. The temperature was fixed at 22 °C. The steady-shear viscosity, first normal stress difference, and first normal stress coefficient measurements are shown for BF1 in Fig. 2(a) and for BF2 in Fig. 2(b). Results from the transient stress relaxation of the first normal stress difference following a step strain are shown in Fig. 2(c). In Fig. 2(d), the complex viscosity measurement during a small-amplitude oscillatory shear test is shown. The rheological fit

TABLE I. FENE-P model parameters.

Fluid	η_0 (Pa s)	β	λ (s)	L^2
BF1	0.97	0.34	0.90	250
BF2	8.70	0.90	1.20	450

of our polymeric fluids using the FENE-P constitutive model is also shown in Fig. 2 and the model parameters are summarized in Table I. The methodology for fitting the FENE-P model to the rheological measurements is as follows. From the small-amplitude oscillatory shear tests [Fig. 2(d)], estimates for the zero-shear viscosity η_0 and solvent viscosity η_s were obtained by looking at the plateau values of the complex viscosity at low- and high-frequency regimes, respectively. The zero-shear viscosity is defined as $\eta_0 = \eta_s + \eta_p$, where η_p is the polymer viscosity. The value for η_0 was confirmed from the steady-shear data. For BF2, η_s was measured from a steady-shear test on a fluid mixture comprised of the same ratio of corn syrup, glycerol, and water, but without the polyacrylamide. The solvent contribution to the viscosity $\beta = \eta_s/\eta_0$ could then be calculated for both fluids. To estimate a characteristic polymer relaxation time, the decay in the primary normal stress [Fig. 2(c)] was fit to a single-exponential curve at long times to characterize the fluid's longest relaxation time. The remaining fitting parameter L^2, which represents the finite maximum extensibility of the polymer [6], was fit by minimizing error between the model and the steady-shear data.

B. Experimental apparatus

In our experiments, we examine the sedimentation of a dense rigid sphere in a concentric cylinder apparatus (or Taylor-Couette flow cell), shown in Fig. 3. The inner cylinder had an outer radius of $R_i = 75$ mm and the outer cylinder had an inner radius $R_o = 85$ mm, for a gap size of $W = 10$ mm

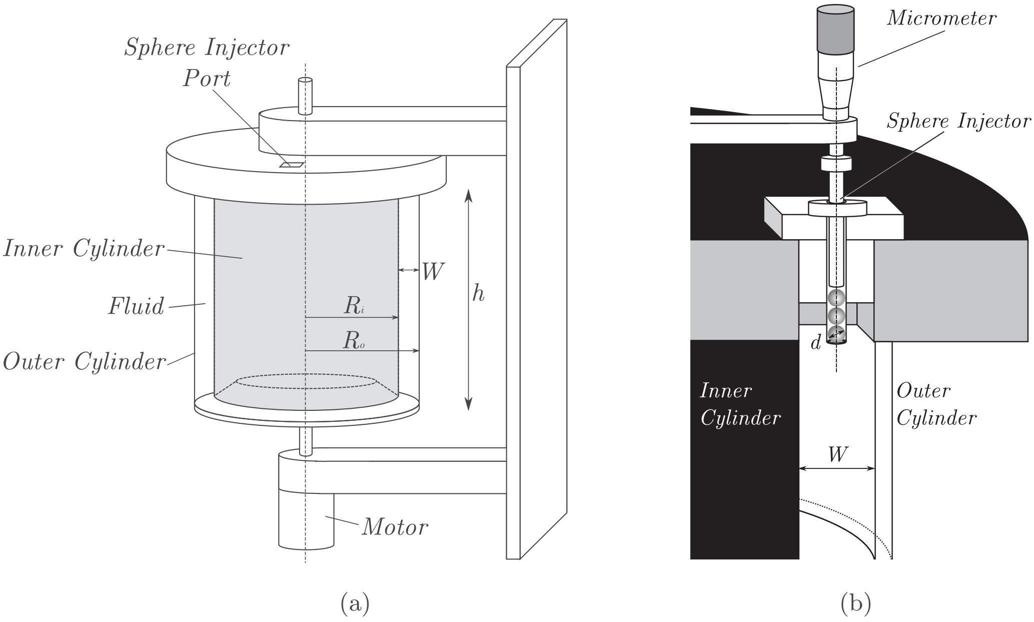

FIG. 3. (a) Experimental Taylor-Couette flow cell used to study the sedimentation of spheres undergoing orthogonal shear flow. (b) Cross-sectional view of the sphere injector that enabled precise release of the spheres along the centerline of the concentric-cylinder gap.

and a radius ratio of $\kappa = R_i/R_o = 0.88$. The height of the cylinders was $h = 150$ mm. Rotation of the cylinders was controlled via PC-operated motor drives (Compumotor CPHX106-220). In these experiments, the outer cylinder was rotated while the inner cylinder remained stationary. The volume between the two cylinders was filled with the viscoelastic fluid discussed in Sec. III A. Spheres of varying radius a and density $\rho_s = 2790\ \mathrm{kg/m^3}$ (aluminum spheres) and $\rho_s = 4430\ \mathrm{kg/m^3}$ (titanium spheres) were then released directly at the center of the gap. A confinement ratio ϵ can be defined based on the sphere diameter and cylinder gap width $\epsilon = 2a/W$. The outer cylinder, made of transparent acrylic, allowed for video observation of the sphere trajectory and subsequent calculation of its settling rate. For higher shear rates, two cameras were used (facing the front and back sides of the cell) as the sphere translated with the shear flow. Settling rates were calculated once spheres reached their terminal velocity. Each reported settling rate is the average of three measurements, with standard deviations in the measurement for all trials within 7% of the mean (error bars shown on plots of the sphere settling rate, shown later in Sec. IV, represent one standard deviation). Note that for these experiments, the particle Reynolds number $\mathrm{Re}_p = \rho_f U_{\mathrm{sed}} 2a/\eta$ was less than 0.15 and the elasticity number $\mathrm{El} = \lambda\eta_0/\rho_f a^2$ was greater than 100 and we anticipate that inertial forces are negligible compared to viscous and elastic forces.

To ensure that spheres were released directly at the centerline of the concentric-cylinder gap with minimal downward momentum, a sphere injector was constructed as shown in Fig. 3(b). A tube of radius $a_{\mathrm{tube}} \approx a(1-\delta)$, where $\delta \ll 1$, held the spheres, while a plunger was slowly depressed using a micrometer screw, releasing the spheres gently into the fluid. Special caution was taken to avoid bubble attachment to the spheres; the tube was prefilled with fluid and the spheres were released beneath the surface of the fluid. The sphere injector was held stationary in the sphere injector port, at the centerline of the gap $W/2$. Migration of spheres suspended in viscoelastic fluids in cylindrical Couette flow has been well described by D'Avino *et al.* [42,43]. These authors, using experiments and numerical simulations, showed evidence for sphere migration in shear thinning fluids but did not observe significant migration in Boger fluids with large solvent contributions to the overall viscosity. For BF1, although the fluid is modestly shear thinning with a significant polymer contribution to the viscosity ($\beta = 0.34$), the sedimentation velocities from our experiments were much larger than the migration velocities observed by D'Avino *et al.* [42], so we would not expect significant cross-stream migration to occur during the course of the sedimentation trials. For BF2, the solvent contribution to the viscosity is very high ($\beta = 0.90$), so we would again not expect significant cross-stream migration to occur.

The Taylor-Couette flow cell was not temperature controlled so the fluid temperature varied during experiments by up to 2 °C. To account for this, the viscosity of the fluid was measured as a function of temperature within this range and a viscosity-temperature relationship $\eta = \eta(T)$ was generated. Results for the sedimentation velocity at a given $T = T_{\mathrm{meas}}$ were adjusted to their assumed sedimentation velocity at $T_0 = 22\,^{\circ}\mathrm{C}$ based on a Stokes law correction, using the expression $U(T_0) = U(T)\eta(T)/\eta(T_0)$. We neglect the effects of any change in the fluid's elastic properties in this small temperature range.

IV. RESULTS

A. Sedimentation velocities and drag

The terminal settling velocities, shown in dimensionless form as the sedimentation Weissenberg number $\Theta = U_{\mathrm{sed}}\lambda/2a$, are compared in Fig. 4 between experiments and simulations for different confinement ratios ($\epsilon = 2a/W$). The simulations predict the reduction in settling velocity and mobility, or increase in drag, with increasing shear Weissenberg number $\mathrm{Wi} = \lambda\dot{\gamma}$ (where $\dot{\gamma}$ is the shear rate). At $\mathrm{Wi} = 0$, the fluid is quiescent, and increasing Wi represents an increasing orthogonal shear rate, since we assume that at all shear rates the longest fluid relaxation time remains constant. The increase in sphere drag is observed across a range of sphere sizes ($\epsilon = 0.16, 0.32, 0.48$) and sphere densities ($\rho_s = 2790, 4430\ \mathrm{kg/m^3}$). The sphere density dictates the body force on the sphere and so Figs. 4(a) and 4(b) show a range of forcing on the sphere, which is indirectly represented by

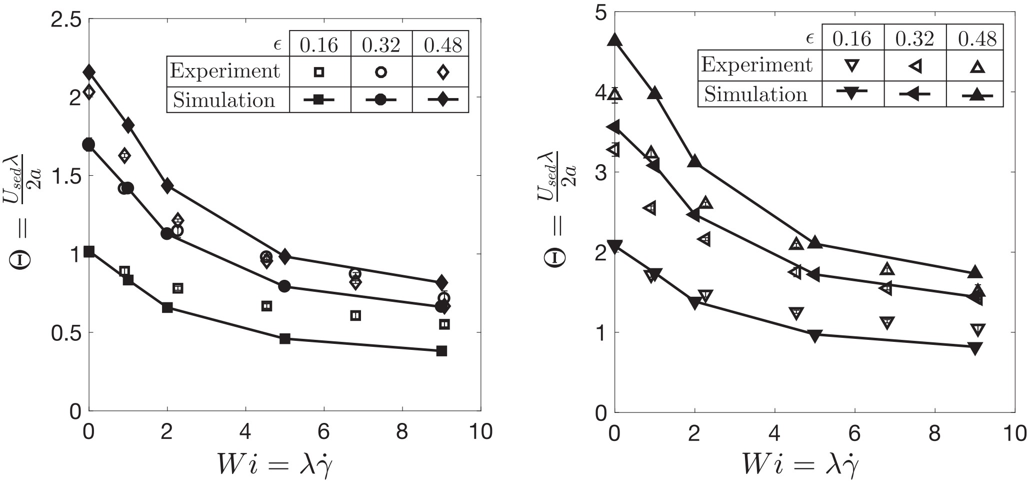

(a) (b)

FIG. 4. Experimentally measured settling velocities (open symbols) with corresponding simulation results (lines with closed symbols) plotted versus shear Weissenberg number for BF1, across a range of particle confinement ratios $\epsilon = 2a/W$ for (a) aluminum spheres and (b) titanium spheres.

$\Theta_0 = \Theta(\mathrm{Wi} = 0)$. Note that both the sedimentation Weissenberg number Θ and the shear Weissenberg number Wi, which are ratios of the polymer relaxation time scale to the flow time scale in the settling direction and the shear direction, respectively, are $O(1)$. We observe reasonable agreement between the numerical simulations and experiments. These numerical simulations thus allow us to explore the mechanism that is responsible for the increase in drag.

In Fig. 5(a), we show the sphere's rotation rate, made dimensionless by $\dot{\gamma}$, as a function of Wi. The results shown are from numerical simulations. In an unbounded Newtonian fluid, a rotational velocity

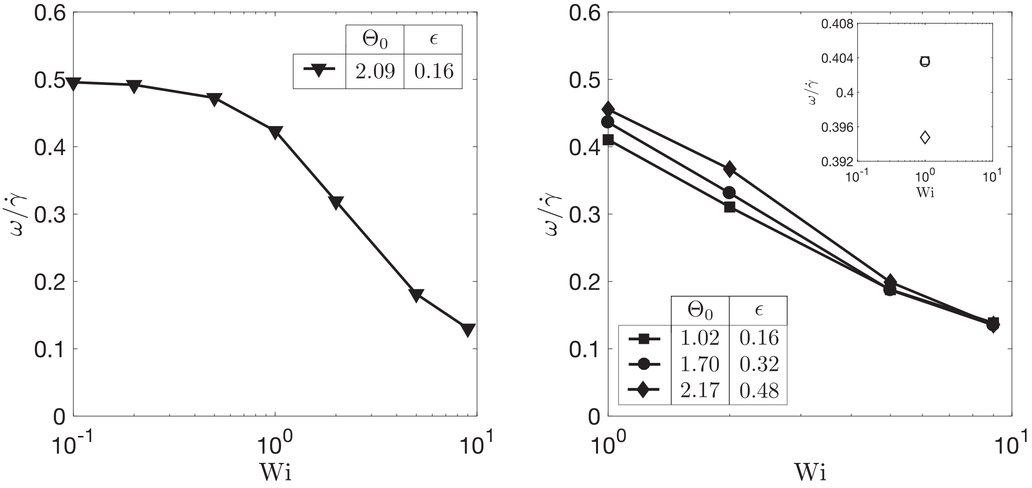

(a) (b)

FIG. 5. Rotation rate from simulation plotted versus shear Weissenberg number for BF1: (a) effect of viscoelasticity on the rotation rate of a settling sphere and (b) effect of confinement ratio ϵ and forcing Θ_0 on the rotation rate of a settling sphere. The inset of (b) shows the rotation rate of confined spheres at $\Theta_0 = 0$ (neutrally buoyant spheres).

of $\omega/\dot{\gamma} = 0.5$ is expected. As observed in Fig. 5(a), we see an overall decrease in the normalized rotational velocity $\omega/\dot{\gamma}$, signifying an increasing deviation from the Newtonian prediction, as Wi increases. Note that the rotational velocity of the sphere ω (in dimensional terms) increases as a function of Wi. This qualitatively matches the results observed in Boger fluids for neutrally buoyant spheres in a viscoelastic shear flow [14,17].

In Fig. 5(b), the sphere's rotation rate is plotted again as a function of Wi for Wi $\geqslant 1$ and is shown for a range of confinement ratios ϵ and sphere forcing Θ_0 obtained from simulation. Interestingly, we observe an increase in the sphere's rotation rate as ϵ and Θ_0 are increased at a fixed Wi. Previously, it has been shown that confinement decreases the rotation rate of a neutrally buoyant sphere in a viscoelastic shear flow [44]. However, recall that in our experimental design, the confinement and sphere forcing (or body force) are confounded, since they both increase with sphere radius for a fixed sphere density. In the inset of Fig. 5(b), the rotation rate of a neutrally buoyant sphere ($\Theta = 0$) at Wi $= 1$ is shown, which recovers the trend observed previously [44]. Thus, it appears as though a confined sphere's rotation rate is coupled with its settling motion such that a forced sphere can rotate more quickly than an equivalent neutrally buoyant sphere in this parameter regime. This coupling effect on the torque is perhaps unsurprising, as the remainder of this paper highlights how the coupling between the shear flow and uniform flow past a sphere affects the drag on the sphere.

We return to the sphere's settling motion to better describe the origin of the increased drag on the sphere. For vanishing fluid inertia, a coefficient relating the steady-state settling velocity to the drag force can be written as

$$C = \frac{F_d}{\eta_0 a U_{\text{sed}}}, \tag{5}$$

where F_d is the drag force on the sphere and the Stokes law predicts $C = 6\pi$ for Newtonian fluids. To further study the mechanism of drag increase, we decompose the drag force into contributions from the form (or pressure) drag, viscous drag, and polymer drag. The contributions to this coefficient of drag, as defined in Eq. (5), can be found from simulations by integrating the stress over the surface of the sphere. In dimensionless terms, we can write the total drag as [32,33]

$$C = -2\iint_S p n_1 dS + 2\beta \iint_S \left(\frac{\partial u_1}{\partial x_k} + \frac{\partial u_k}{\partial x_1}\right) n_k dS + 2\frac{1-\beta}{\Theta} \iint_S \sigma^P_{1k} n_k dS, \tag{6}$$

where the three terms above correspond to the form, viscous, and polymer drag, respectively. We have broken down the drag force for different sphere forcing and confinement ratios and plotted the corresponding drag as a function of the shear Weissenberg number in Fig. 6. With increasing shear Weissenberg number, the viscous and form drag components increase, with the form (or pressure) drag dominating at high Wi. The component of drag due to the form drag increases roughly fourfold at Wi $= 9$ for $\epsilon = 0.48$ [Figs. 6(e) and 6(f)], relative to the case with no shear. We observe in this study that for all parameter regimes where $\Theta_0 \sim O(1)$, the form drag is the dominant contribution to the total drag. This is in contrast to the mechanisms proposed for weakly elastic fluids ($\Theta_0 < 1$), reported previously, where either the viscous drag [32] or polymer tension [27] is suggested to be primarily responsible for an increase in the total drag.

From Fig. 6 it is clear that the form drag is the dominant contribution to the total drag in this parameter range, but it is difficult to discern the effects of Wi, Θ_0, and ϵ. In the next section, we will introduce a model to isolate and quantify the coupling drag, i.e., the drag from the coupling of the orthogonal shear flow and the uniform flow past the sphere. This will allow us to study the coupling drag consistently across a range of Θ_0 and ϵ and estimate their effects on the coupling drag. This will also allow us to observe how the coupling drag scales with Wi.

B. Coupling drag

In this section, we introduce a model force balance in order to elucidate the effect of orthogonal shear on particle sedimentation in a viscoelastic fluid. Assuming a sphere of radius a and density

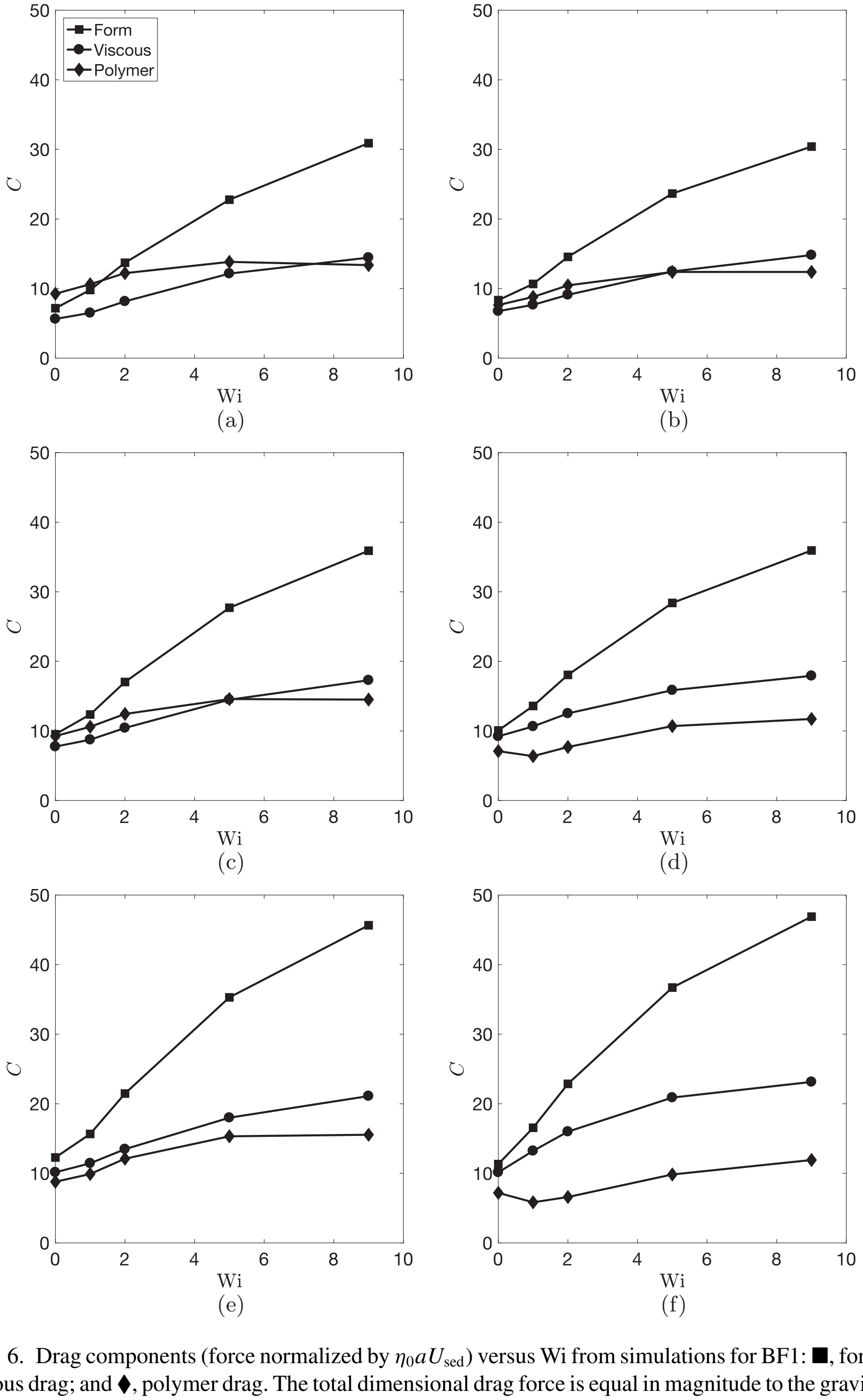

FIG. 6. Drag components (force normalized by $\eta_0 a U_{\text{sed}}$) versus Wi from simulations for BF1: ■, form drag; ●, viscous drag; and ♦, polymer drag. The total dimensional drag force is equal in magnitude to the gravitational body force (minus buoyancy) at steady state and constant for all Wi within a plot. Results are shown across a range of ϵ and Θ_0, corresponding to (a), (c), and (e) aluminum spheres, $\rho_S = 2790\,\text{kg/m}^3$, and (b), (d), and (f) titanium spheres, $\rho_S = 4430\,\text{kg/m}^3$: (a) $\epsilon = 0.16$ and $\Theta_0 = 1.02$, (b) $\epsilon = 0.16$ and $\Theta_0 = 2.09$, (c) $\epsilon = 0.32$ and $\Theta_0 = 1.70$, (d) $\epsilon = 0.32$ and $\Theta_0 = 3.58$, (e) $\epsilon = 0.48$ and $\Theta_0 = 2.17$, and (f) $\epsilon = 0.48$ and $\Theta_0 = 4.65$.

ρ_s is sedimenting in a quiescent viscous fluid of viscosity η and density ρ_f, then at steady state the force balance is simply the Stokes drag force balanced with the gravitational force (minus buoyancy) $6\pi\eta aU = \frac{4\pi}{3}(\rho_s - \rho_f)a^3 g$. In a quiescent viscoelastic fluid, a correction to the drag may be added to account for the effect of fluid elasticity. In the following expression, $C_e(\mathrm{Wi} = 0,\Theta_0)$ represents the effect of fluid elasticity on the fluid drag in the absence of shear:

$$6\pi\eta aU + C_e(\mathrm{Wi} = 0,\Theta_0)U = \tfrac{4}{3}\pi\Delta\rho a^3 g. \tag{7}$$

Other studies have expressed this equivalently as a viscoelastic correction to the drag coefficient $K_{VE}6\pi\eta aU = \frac{4}{3}\pi\Delta\rho a^3 g$, where $K_{VE} = 1 + C_e/6\pi\eta a$. This correction may be measured from simple sedimentation in quiescent fluids and has been studied experimentally, theoretically, and via numerical simulation [8–10]. Interestingly, $C_e(\mathrm{Wi} = 0,\Theta_0)$ may be of either sign and it may vary nonmonotonically as a function of Θ_0 [8,10] (other authors denote K_{VE} by X or Y). For certain (mostly unconfined) Boger fluids, C_e has been shown to be negative for $\Theta_0 < 1$, eventually becoming positive and growing at higher Θ_0, as elastic effects in the wake become dominant, as alluded to in Sec. I. Additionally, it can change based on the fluid properties, including the solvent quality [45].

For a sphere now sedimenting in a viscoelastic fluid under orthogonal shear, we introduce a further correction to the drag, where we have allowed the viscosity (and settling velocity) to vary with orthogonal shear rate,

$$6\pi\eta(\dot{\gamma})aU + C_e(\mathrm{Wi} = 0,\Theta_0)U + C_c(\mathrm{Wi},\Theta_0)U = \tfrac{4}{3}\pi\Delta\rho a^3 g. \tag{8}$$

The first term on the left-hand side represents the effect of shear in the absence of elasticity on the viscosity via a modified Stokes law, the second term represents the effect of elasticity in the absence of shear, i.e., the extra drag due to elasticity with no orthogonal shear, and the third term is defined as the coupling drag associated with shear and sedimentation. The focus of this work is on the coupling drag, where we seek to find the functionality of C_c on Wi and Θ_0. Rearranging our expression,

$$\bar{C}_c = \frac{C_c(\mathrm{Wi},\Theta_0)}{6\pi\eta(\dot{\gamma})a + C_e(\mathrm{Wi} = 0,\Theta_0)} \sim f(\mathrm{Wi},\Theta_0). \tag{9}$$

Perturbation theory suggests scaling in the form

$$\bar{C}_c \sim f\big(k_1\mathrm{Wi}^n, k_2\Theta_0^m\big), \tag{10}$$

where Housiadas and Tanner [24] have shown $n = m = 2$ and $|k_1| \gg |k_2|$ for small $\Theta_0 \ll 1$. This theory was later taken to $O(\mathrm{Wi}^4,\Theta_0^4)$ by Housiadas [25], showing better prediction of the drag increase compared to numerical simulations by Padhy *et al.* [32] up to $\mathrm{Wi} \approx 1$. A simplified model force balance was performed by Tanner *et al.* [27], showing that the drag should scale quadratically in Wi for small Θ_0 and proposing a mechanism based on tension from normal stresses that act along the streamlines deformed around the sedimenting sphere.

The analysis thus far has considered the case of a sphere sedimenting under orthogonal shear in an unbounded viscoelastic fluid. In both our experiments and numerical simulations, the sphere is confined by the shearing walls. We therefore can modify Eqs. (8) and (9), taking into account the effect of confinement. We define our confinement based on the confinement parameter $\epsilon = 2a/W = d/W$, where $W = L_y$ is the distance between our shearing walls. Furthermore, we reintroduce a correction to the Stokes drag $K_N(\epsilon)$, which is known for Newtonian fluids [18,21,22]. We rewrite our force balance in Eq. (11) and rearrange to define a dimensionless form of the coupling drag $\tilde{C}_c$ in Eq. (12),

$$6\pi K_N(\epsilon)\eta(\dot{\gamma})aU + C_e(\mathrm{Wi} = 0,\Theta_0,\epsilon)U + C_c(\mathrm{Wi},\Theta_0,\epsilon)U = \tfrac{4}{3}\pi\Delta\rho a^3 g, \tag{11}$$

$$\tilde{C}_c = \frac{C_c(\mathrm{Wi},\Theta_0,\epsilon)}{6\pi K_N(\epsilon)\eta(\dot{\gamma})a + C_e(\mathrm{Wi} = 0,\Theta_0,\epsilon)} = \frac{\frac{4}{3}\pi\Delta\rho a^3 g}{6\pi K_N(\epsilon)\eta(\dot{\gamma})aU + C_e(\mathrm{Wi} = 0,\Theta_0,\epsilon)U} - 1. \tag{12}$$

In Fig. 7, we show the dimensionless elastic drag $\tilde{C}_e = C_e(\mathrm{Wi} = 0,\Theta_0,\epsilon)/6\pi K_N(\epsilon)\eta a$ versus sedimentation Weissenberg number Θ_0 from experiment and simulation. Also plotted in Fig. 7 are

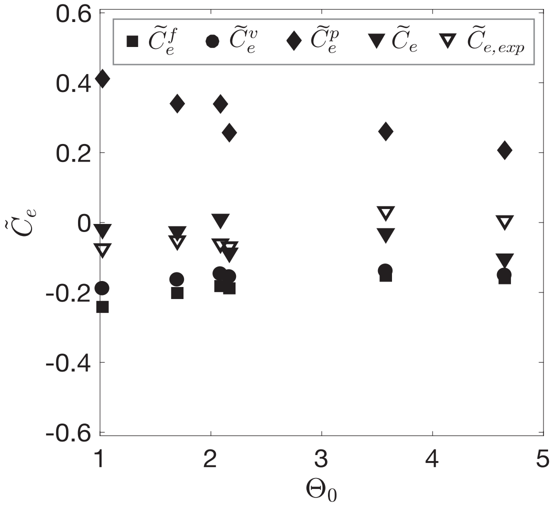

FIG. 7. Elastic drag components $\tilde{C}_e$ plotted versus Θ_0, from simulation: ■, form contribution to the elastic drag; ●, viscous contribution to the elastic drag; ◆, polymer contribution to elastic drag; ▼, overall elastic drag; and ▽, overall elastic drag (experiment).

the contributions to the total elastic drag from the form drag, viscous drag, and polymer drag, as calculated from the simulations. It should be noted that these results are obtained across a range of confinement ratio $\epsilon = 0.16, 0.32, 0.48$. The elastic drag remains roughly constant and small ($\tilde{C}_e \ll 1$) across the range of Θ_0 and confinement tested in this study. To calculate the components of the drag, the contributions to the total drag are found by integrating the stress over the surface of the sphere, similar to Eq. (6). The force balance (in dimensional form) then becomes

$$\left(\frac{F_d^f}{F_d^f + F_d^v}\right)_{\mathrm{Wi}=0} 6\pi K_N(\epsilon)\eta(\dot{\gamma})aU + C_e^f(\mathrm{Wi}=0,\Theta_0,\epsilon)U + C_c^f(\mathrm{Wi},\Theta_0,\epsilon)U = F_d^f, \tag{13}$$

$$\left(\frac{F_d^v}{F_d^f + F_d^v}\right)_{\mathrm{Wi}=0} 6\pi K_N(\epsilon)\eta(\dot{\gamma})aU + C_e^v(\mathrm{Wi}=0,\Theta_0,\epsilon)U + C_c^v(\mathrm{Wi},\Theta_0,\epsilon)U = F_d^v, \tag{14}$$

$$C_e^p(\mathrm{Wi}=0,\Theta_0,\epsilon)U + C_c^p(\mathrm{Wi},\Theta_0,\epsilon)U = F_d^p, \tag{15}$$

where the superscripts denote form (f), viscous (v), or polymer (p) contributions. Thus, for example, F_d^f is the form contribution to the total (dimensional) drag force and C_e^v is the viscous contribution to the elastic drag. At $\mathrm{Wi} = 0$ (e.g., to calculate the elastic drag components for Fig. 7), the coupling drag terms are equal to zero.

The coupling drag is shown in Fig. 8 versus shear Weissenberg number for a range of particle sizes, from both simulation and experiment. The coupling drag is positive and increases monotonically as a function of Wi, up to a factor of over 2 at the highest tested Wi (recall that $\tilde{C}_c$ is normalized by the sum of the wall-corrected Stokes drag and the elastic drag). This trend is observed at $\epsilon = 0.16, 0.32, 0.48$, across a range of Θ_0. For finite $\mathrm{Wi} > 1$, the coupling drag becomes a significantly larger effect than the elastic drag (shown previously in Fig. 7). We observe that for the highly elastic fluid investigated here, the coupling drag is a strong function of Wi and a weaker function of Θ_0 and ϵ. In fact, we see only a small variation in the trend of the coupling drag across a wide range of sphere forcing and particle confinement ratios from the simulations. Experiments show a small but inconsistent effect of Θ_0 at various confinement ratios and a stronger effect of confinement ratio.

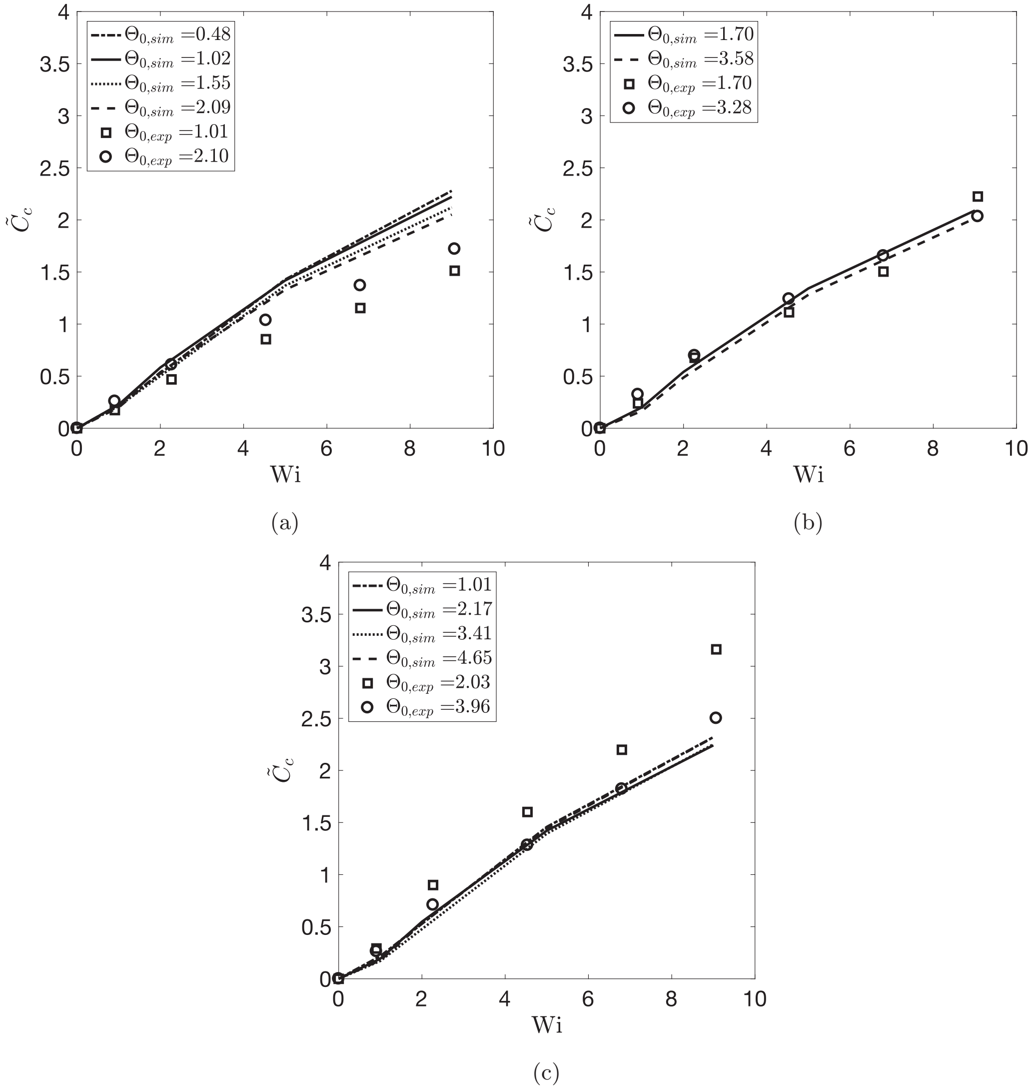

(a)

(b)

(c)

FIG. 8. Coupling drag $\tilde{C}_c$ versus shear Wi for (a) $\epsilon = 0.16$, (b) $\epsilon = 0.32$, and (c) $\epsilon = 0.48$ for various values of Θ_0, from experiment (open symbols) and simulation (lines).

The coupling drag can also be further broken down into the components of drag corresponding to form, viscous, and direct polymer contributions, as shown in Eqs. (13)–(15). The results are shown in Fig. 9 for $\epsilon = 0.16$ and $\epsilon = 0.48$. We observe that the qualitative trends in the coupling drag are consistent across the range of parameters studied here, similar to what was observed for the overall coupling drag. The viscous and form drag contribute most strongly to the coupling drag, with both growing monotonically as a function of Wi. For all parameter ranges studied here, the form coupling drag was the dominant contribution to the overall coupling drag, more than doubling the contribution from the viscous coupling drag at high Wi. The direct polymer contribution to the coupling drag grows only slightly as the orthogonal shear rate increases. Thus, as originally described by Padhy *et al.* [32], the polymers in the fluid indirectly result in an enhanced coupling drag by modifying the flow past the sphere such that the form and (solvent) viscous drag are increased, although the direct polymer contribution to the drag is proportionally diminished. This indirect effect was also

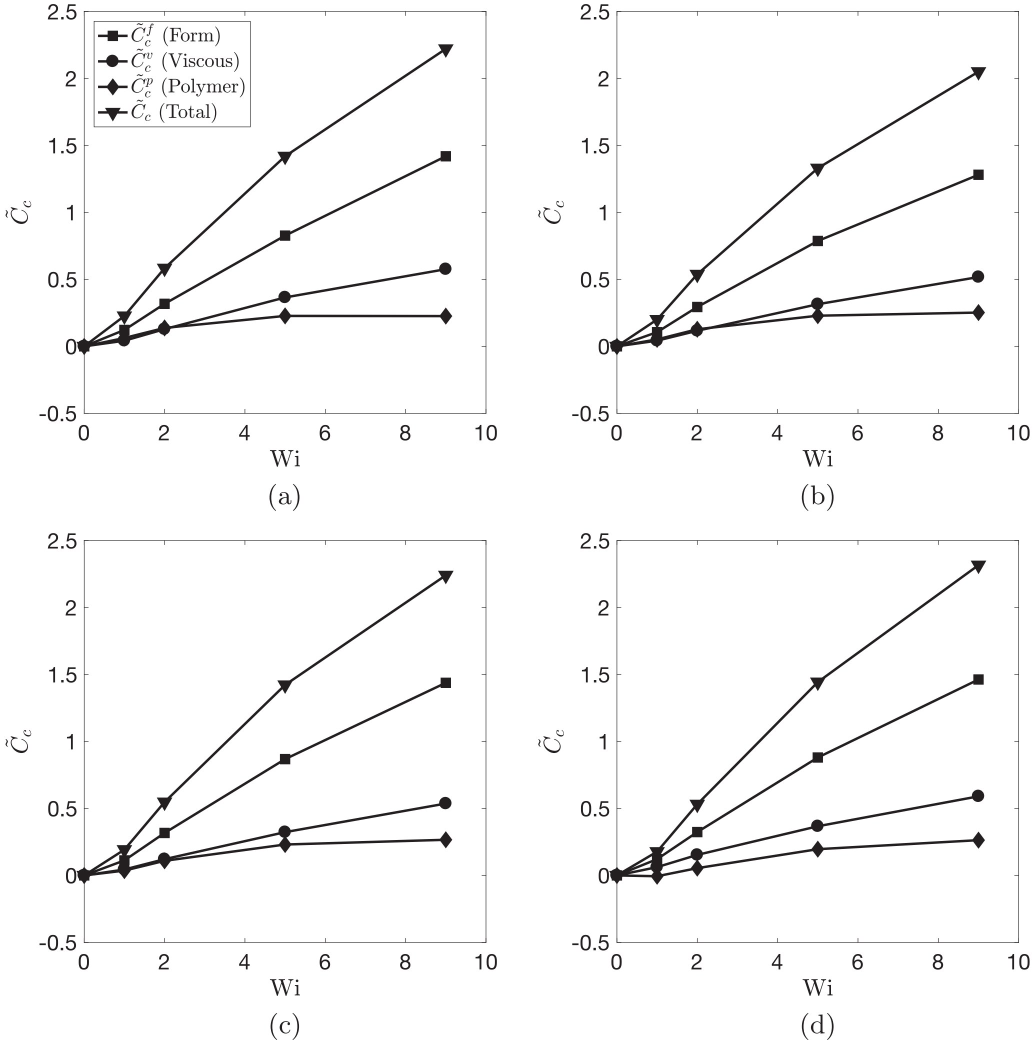

(a) (b) (c) (d)

FIG. 9. Coupling drag components versus shear Wi, from simulation, for (a) $\epsilon = 0.16$ and $\Theta_0 = 1.02$, (b) $\epsilon = 0.16$ and $\Theta_0 = 2.09$, (c) $\epsilon = 0.48$ and $\Theta_0 = 2.17$, and (d) $\epsilon = 0.48$ and $\Theta_0 = 4.65$ for BF1: ▼, total coupling drag; ■, form drag; ●, viscous drag; and ◆, polymer drag.

suggested from perturbation theory [24,26]. Later, in Sec. V, we will examine how the flow field around the settling sphere is modified by the presence of the polymers.

We have thus far described the coupling drag as a function of at least the shear and sedimentation Weissenberg numbers and the confinement ratio $\tilde{C}_c \sim f(\mathrm{Wi}, \Theta_0, \epsilon)$. For $\Theta_0 \sim O(1)$, we have shown that $\tilde{C}_c$ is most strongly a function of the shear Weissenberg number Wi and a weaker function of Θ_0 and ϵ. In Fig. 10, we show $\tilde{C}_c$ vs Wi for a particular value of Θ_0 and ϵ, now shown on a log-log plot to examine the scaling behavior. We observe quadratic growth of $\tilde{C}_c$ at low Wi, transitioning to linear growth at high Wi. This trend is observed for the overall coupling drag, as well as the form and viscous contributions to the coupling drag. The quadratic growth in the coupling drag at lower Wi may be related to the growth in normal stress and the associated tension acting along shear flow streamlines, as suggested previously for $\Theta_0 \ll 1$ [24,27]. However, this would assume that the resistance to flow due to the growing normal stress in the fluid shows up indirectly as increasing form and viscous drag. Further discussion of a mechanism for the increase in the form coupling

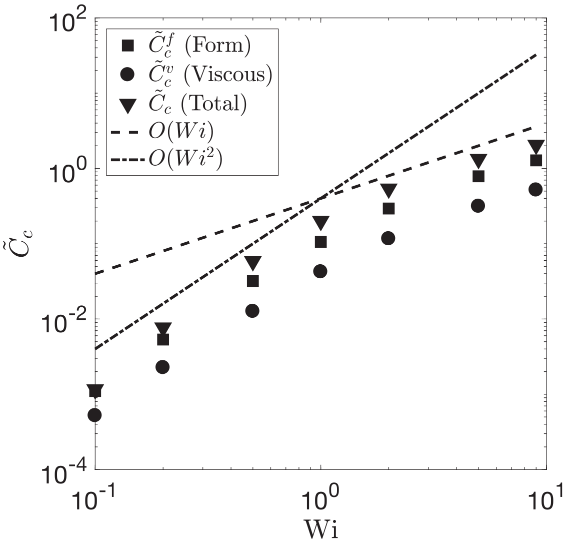

FIG. 10. Coupling drag scaling from simulation for BF1, showing quadratic growth at low Wi and linear growth at high Wi for $\Theta_0 = 2.09$ and $\epsilon = 0.16$.

drag, particularly at high Wi, will be discussed in Sec. V. First, in the following section, Sec. IV C, we will present the results for the settling rate and drag on a sphere settling in a weakly elastic fluid under orthogonal shear and compare it to the results presented here.

C. Weakly elastic fluids

Thus far, we have addressed the drag on a sphere settling in a highly elastic fluid under orthogonal shear. By highly elastic we mean that the motion associated with the applied force on the sphere creates a large deformation of the polymers, i.e., $\Theta_0 \sim O(1)$. In this section, we present results from a sphere settling in a weakly elastic fluid under orthogonal shear ($\Theta_0 < 1$), using BF2 as our model fluid. We show results for the settling rate, total drag, and coupling drag. We discuss the primary contributions to the coupling drag and compare to the contributions presented above for highly elastic fluids. In this manner, we connect the present work to previous work performed for $\Theta_0 < 1$ [24–27,32,33].

Figure 11 shows results for the steady-state velocity of spheres settling in BF2, from experiments and numerical simulations. Both experiments and simulations predict a decrease in the dimensionless settling rate Θ as the orthogonal shear rate Wi is increased. There is reasonable agreement between the simulation and experiment at Wi = 0, with error of $O(10\%)$, in line with comparisons shown in Sec. IV A and in the literature [34]. The discrepancy between simulation and experiment grows at increasing Wi, particularly for the higher-Θ_0 trial. This may be due to the challenges in modeling this fluid with a single longest relaxation time as measured from shear rheology experiments.

The components of drag on a sphere settling in BF2 are shown in Fig. 12, as calculated from Eq. (6). For BF2, the solvent contribution to the total viscosity is relatively high ($\beta = 0.90$). Thus, at Wi = 0 and low Θ_0, we see a small contribution from the polymer drag, and viscous and form drag contributions that are close to that for a Newtonian fluid: $C^v \approx 4\pi$ and $C^f \approx 2\pi$ (once correcting for the confinement). With increasing shear Weissenberg number Wi, the viscous and form drag increase, with the viscous drag increase becoming dominant at high Wi; this is in contrast to what was observed previously for highly elastic fluids, where the form drag was the dominant component. Further insight is achieved by looking at the coupling drag, as introduced in Sec. IV B.

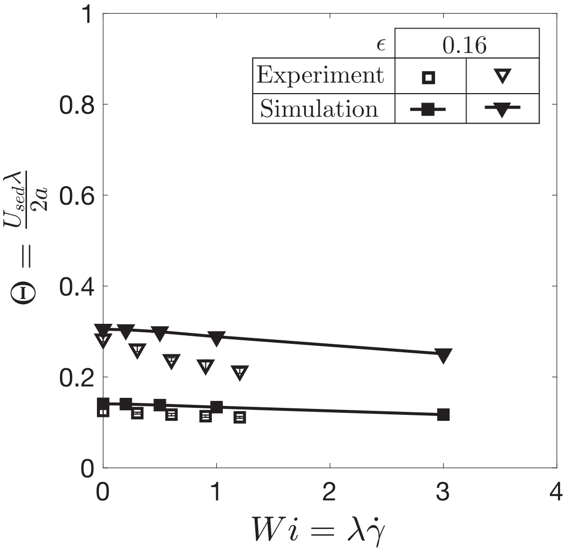

FIG. 11. Experimentally measured settling velocities (open symbols) with corresponding simulation results (lines with closed symbols) plotted versus shear Weissenberg number for BF2.

The overall and componentwise coupling drag is shown in Fig. 13. We see that at low-shear Weissenberg number Wi < 1, the viscous and form drag contributions to the coupling drag are roughly equivalent. This is in qualitative agreement with the predictions for the components of drag made by Housiadas and Tanner [26] for low-Weissenberg-number regimes where $\Theta_0 \ll 1$ and Wi < 1. However, we do not see a drop in the viscous drag above a critical Wi, but rather a

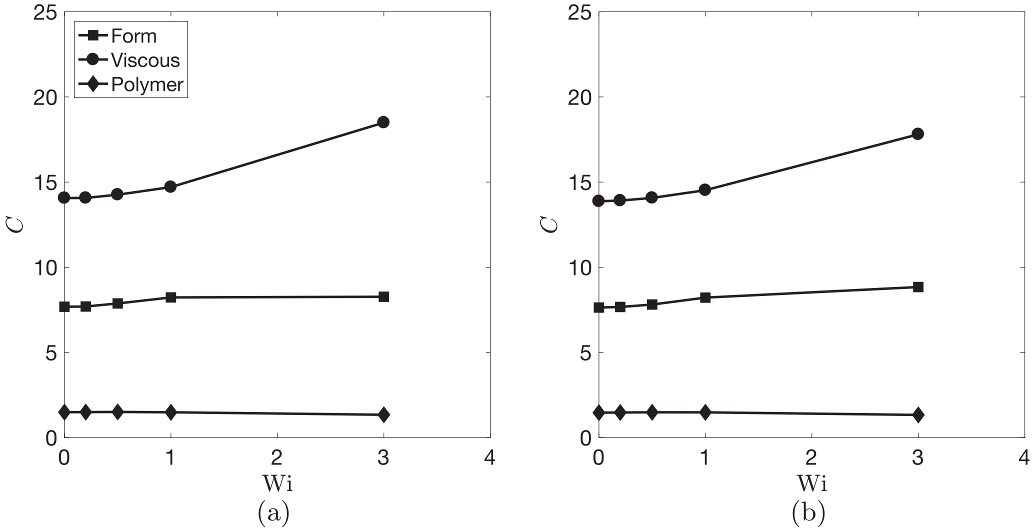

(a)

(b)

FIG. 12. Drag components (force normalized by $\eta_0 a U_{\mathrm{sed}}$) from simulations for (a) $\epsilon = 0.16$ and $\Theta_0 = 0.14$ and (b) $\epsilon = 0.16$ and $\Theta_0 = 0.30$ for BF2: ■, form drag; ●, viscous drag; and ◆, polymer drag. The total dimensional drag force is equal in magnitude to the gravitational body force (minus buoyancy) at steady state and constant for all Wi within a plot. Results are shown for (a) aluminum spheres, $\rho_S = 2790\,\mathrm{kg/m^3}$, and (b) titanium spheres, $\rho_S = 4430\,\mathrm{kg/m^3}$.

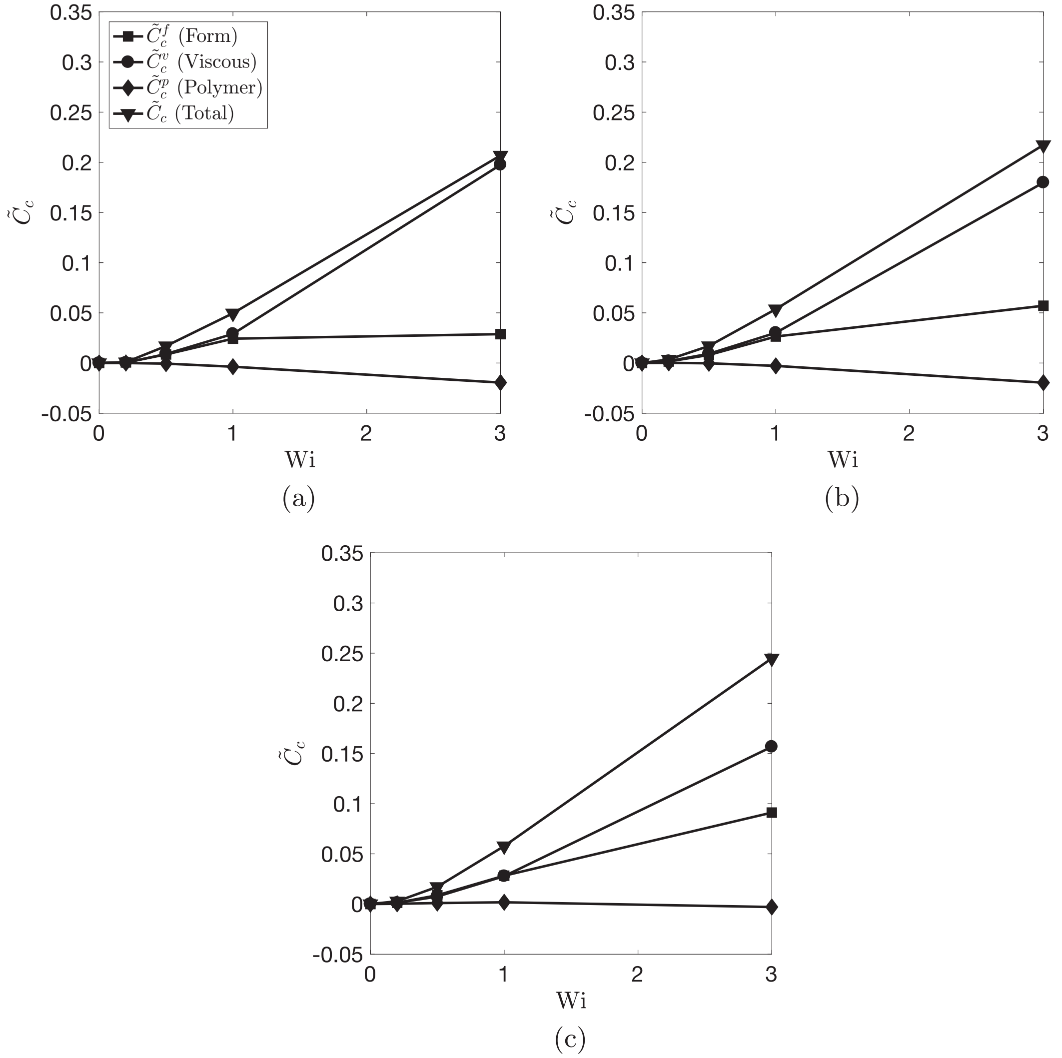

FIG. 13. Coupling drag components versus shear Wi for (a) $\epsilon = 0.16$ and $\Theta_0 = 0.14$, (b) $\epsilon = 0.16$ and $\Theta_0 = 0.30$, and (c) $\epsilon = 0.16$ and $\Theta_0 = 0.66$ for BF2: ▼, total coupling drag; ■, form drag; ●, viscous drag; and ◆, polymer drag.

further increase in the viscous drag at increasing Wi. In fact, the viscous drag continues to grow and becomes the dominant contribution to the coupling drag at increasing Wi. At lower Θ_0, e.g., Figs. 13(a) and 13(b), the form drag appears to plateau. At higher Θ_0, e.g., Fig. 13(c), the form drag increases nearly with the viscous drag at increasing Wi, contributing to a higher total coupling drag relative to lower-Θ_0 trials. The increasing contribution from the form drag at increasing Θ_0 and Wi appears to be in accord with the observations above for a highly elastic fluid, where the form drag was the dominant contribution to the drag.

V. DISCUSSION

In the following section, we start by summarizing our results in Sec. V A. In Sec. V B, we discuss a mechanism for the observed coupling drag in highly elastic fluids [$\Theta_0 \sim O(1)$]. In doing so, we delve into the microstructural origins of the coupling drag and we investigate the viscoelastic wake structure that forms behind a sphere settling under orthogonal shear in a viscoelastic fluid. We examine how this wake structure changes the flow field around the sphere and propose an explanation for the enhanced coupling drag. Finally, in Sec. V C, we compare our discussion in Sec. V B to the physical mechanism for the increase in the drag in orthogonal shear in weakly elastic fluids ($\Theta_0 < 1$).

A. Summary of findings

In Sec. IV, we introduced a model force balance to describe the coupling drag, a drag associated with sedimentation and an orthogonal shear in a viscoelastic fluid. We proposed that the coupling drag was a function of at least the shear and sedimentation Weissenberg numbers and the confinement ratio $\tilde{C}_c \sim f(\mathrm{Wi},\Theta_0,\epsilon)$. For all parameter regimes studied here, the coupling drag monotonically grew with Wi. It was shown that although the coupling drag is enabled by the presence of polymers in the carrier fluid, it is not directly due to polymer stress on the sphere surface. Instead, we observe that the coupling drag is primarily driven by the growth of either the form or viscous drag on the sphere, suggesting that the polymers contribute to an off-surface modification of the flow around the sphere. For highly elastic fluids, where $\Theta_0 \sim O(1)$, we observe that the coupling drag at increasing Wi was dominated by the form drag. The effects of sphere forcing and confinement on the coupling drag were relatively small compared with the effect of Wi. For weakly elastic fluids, where $\Theta_0 < 1$, we observe that the coupling drag growth at increasing Wi was driven by growth primarily in the viscous drag.

In order to study $\Theta_0 \sim O(1)$ and $\Theta_0 < 1$ regimes, we used two separate Boger fluids with different rheological properties. Our discussion of the results would be incomplete without addressing the effect of the solvent contribution to the viscosity $\beta = \eta_s/(\eta_s + \eta_p)$ on our results. Previously, Housiadas and Tanner [24] showed with perturbation theory ($\Theta_0 \ll 1$) that the drag increase due to an orthogonal shear flow is enhanced at lower β (i.e., for higher polymer contribution to the viscosity) in an Oldroyd-B fluid. Padhy *et al.* [32] discussed the effect of β on the drag in shear thinning guar gum fluids at low Θ, showing that a small enough β can reduce the total drag due to a shear thinning viscosity. However, by accounting for the reduction in bulk viscosity due to shear thinning, they concluded that β did not change the fundamental mechanism for the elasticity-induced drag increase due to an orthogonal shear. Clearly, we must consider $\tilde{C}_c \sim f(\mathrm{Wi},\Theta_0,\epsilon,\beta)$. In our study, we used Boger fluids with only modest shear thinning in the range of shear rates tested, but the values of β were dissimilar for the two fluids. We showed that in BF1, with a low solvent contribution to the total viscosity $\beta = 0.34$, the form drag was the dominant contribution to the total drag for all values of Θ_0 tested. In BF2, with a high solvent contribution to the viscosity, $\beta = 0.90$, the viscous drag was the dominant contribution to the total drag at low Θ_0. However, as Θ_0 was increased, the form drag contribution to the coupling drag grew and we expect that at high enough Θ_0, the form drag would become the dominant contribution to the coupling drag. Thus, we propose that either a low solvent contribution to the viscosity (low β) or a high sphere forcing [$\Theta_0 \sim O(1)$] can be sufficient for the coupling drag to be dominated by the form drag. In the following section, we will discuss the wake structures that form around a sphere settling in a sheared viscoelastic fluid and how they can contribute to the growth of the coupling form drag.

B. Mechanism in highly elastic fluids

In this section, we study the mechanism for the reduction in particle mobility. First, we look at the case of the largest, most strongly forced sphere ($\epsilon = 0.48$ and $\Theta_0 = 4.65$). We examine the polymer stretching in the vicinity of the sphere in Fig. 14, which shows the isosurfaces of the trace of the conformation tensor at 30% of maximum extensibility. These surfaces represent regions of high polymer deformation and tension exceeding that caused by the background shear flow alone. In a simple shear flow at $\mathrm{Wi} = 9$, the trace of the polymer conformation tensor is approximately 27% of maximum extensibility and thus these isosurfaces were chosen to highlight the interaction between

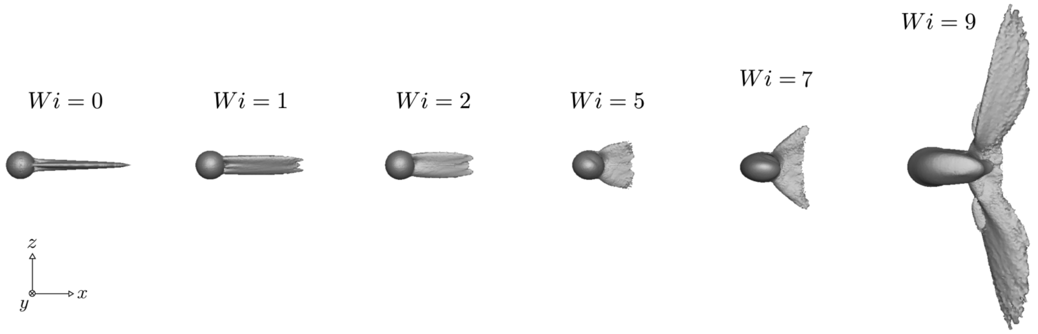

FIG. 14. Isosurface plots of the trace of the conformation tensor at 30% of maximum extensibility, viewed from the y direction, for $\Theta_0 = 4.65$, and $\epsilon = 0.48$.

the fluid flow and the sphere. At $\mathrm{Wi} = 0$, the isosurface is that of a viscoelastic flow past a sphere, with a thin region of stretched polymers in the wake of the sphere, extending from the rear stagnation point along the outgoing (downstream) streamlines [11,13]. At increasing Wi, we observe that the polymer stretching broadens in the direction of shear. At $\mathrm{Wi} > 5$ these structures resemble wings and we refer to these as viscoelastic wings. We choose to describe the wake structures as wings to describe their geometric shape. However, unlike wings, these structures are not mirror symmetric but rather symmetric about an 180° rotation around the x axis. Owing to this symmetry, these wings do not generate lift. Instead, we observe that the increase in the drag is linked to the development of these viscoelastic wings through the deflection of fluid.

In Fig. 15(a), the wake structures for spheres with the confinement ratio $\epsilon = 0.48$ and across a range of sphere forcing are shown. It is observed that as Θ_0 is increased, the wake is progressively stretched and angled back into the $+x$ direction, resembling the wings discussed above. At progressively lower Θ_0, the viscoelastic wake structures flatten and stretch further into the shear direction as the deformation due to the shear flow becomes dominant. In Fig. 15(b), we show that

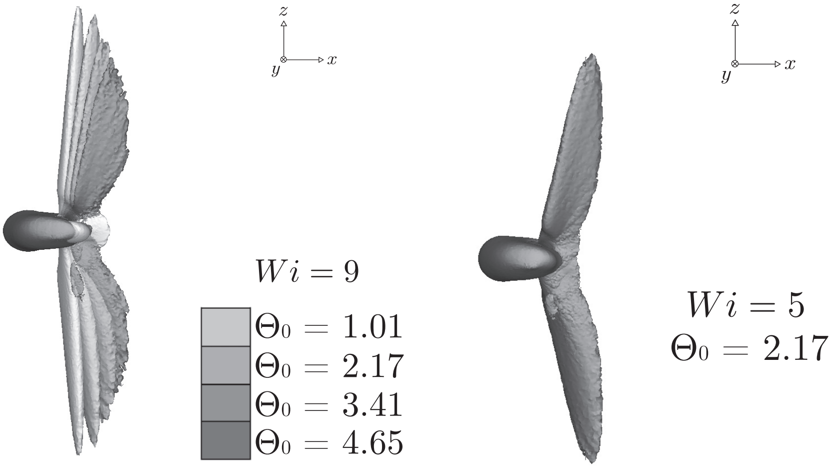

(a)

(b)

FIG. 15. Isosurface plots of the trace of the conformation tensor at (a) 30% of maximum extensibility, as a function of Θ_0 at $\mathrm{Wi} = 9$ and $\epsilon = 0.48$, and (b) 16% of maximum extensibility, at $\Theta_0 = 2.17$, $\mathrm{Wi} = 5$, and $\epsilon = 0.48$.

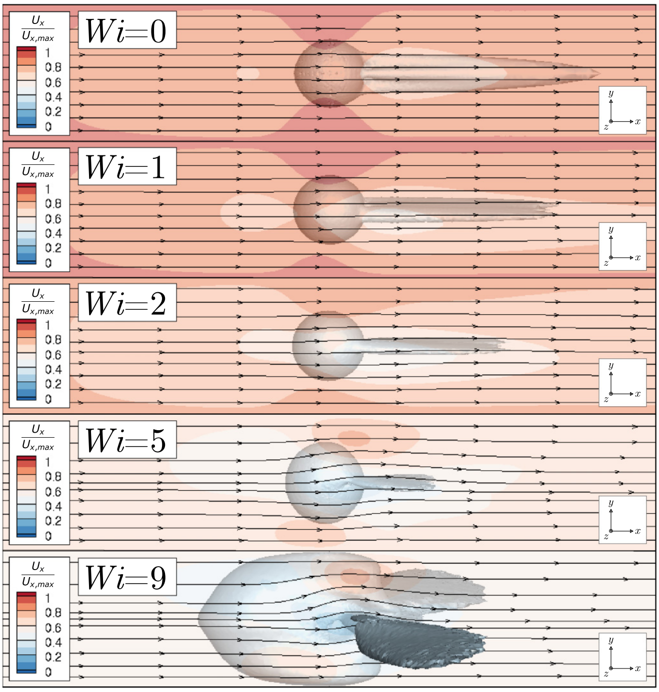

FIG. 16. Isosurface plots of the trace of the conformation tensor at 30% of maximum extensibility, viewed from the z direction, for $\Theta_0 = 4.65$ and $\epsilon = 0.48$. A contour plot slice of $U_x/U_{x,\max}$ at $z = 2a$ (at 40% translucency) is shown. Streamlines of $(U_x, U_y, 0)$, where U_z has been set to zero, are shown in the x-y plane of the slice. The streamlines are seeded at $z = 2a$ and $x = 1.1a$ across a range of y.

this wing shape can be observed at lower Wi for a lower sphere forcing. In this case, at Wi = 5, an isosurface of the trace of the conformation tensor is shown at 16% of maximum extensibility (the background shear flow is approximately 14% of maximum extensibility). By looking at regions of polymer stretch slightly above the background stretch, we can observe qualitatively similar structures across a wide range of $O(1)$ values of Wi and Θ_0, as well as across the range of ϵ studied here (an example of $\epsilon = 0.16$ wake structures is later shown in Fig. 20). It should be mentioned that these values for the Weissenberg number are not extreme cases of deformation in an applied setting. Indeed, this high-Weissenberg-number regime is easily accessible in engineering applications with elastic fluids, including oilfield applications, microfluidics, and 3D printing, where the Weissenberg number can reach $O(1)$–$O(10)$ values or higher. We next investigate how the development of these viscoelastic wake structures affects the flow past the sphere.

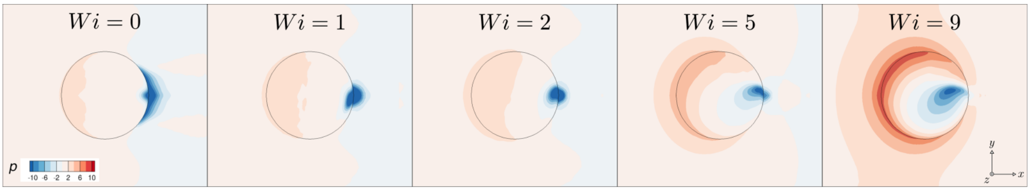

FIG. 17. Contour plots of pressure [minus the hydrostatic pressure and made dimensionless with $U_{\text{sed}}(\text{Wi} = 0)\eta_0/a$] on the surface of the sphere and in a slice at $z = 0$ surrounding the sphere, viewed from the z direction, for $\Theta_0 = 4.65$ and $\epsilon = 0.48$.

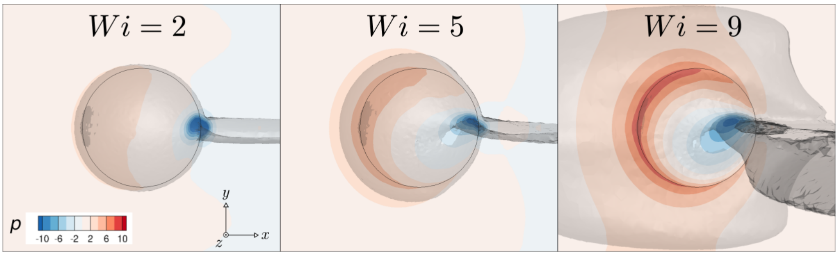

FIG. 18. Contour plots of pressure (as shown in Fig. 17, now with semitranslucent isosurface plots of the trace of the conformation tensor at 30% of maximum extensibility overlaid).

Figure 16 shows a plot of the streamlines in a plane two radii away from the sphere center in the shear flow direction, with the fluid velocity along the shear direction set to zero. At Wi $= 0$, the streamlines are essentially parallel. The streamlines are deflected at higher Wi, particularly near the wings. Thus the wings, depicting areas of high polymer tension, provide a mechanism for flow deflection. This results in regions of high fluid velocity in the x direction above and below the wing and a region of low fluid velocity near the wing (as seen from the contour plot slices). In other words, the flow is modified in the region around the surface of the sphere such that it creates an additional blockage for the fluid, which ultimately contributes to an increase in the pressure drag.

Figure 17 shows the contours of pressure in the vicinity of the sphere. At increasing Wi, we observe the development of a high-pressure region on the front side of the sphere (note that the sphere is sedimenting from right to left). A low-pressure region can also be seen on the back side of the sphere, which shifts slightly to the sides of the sphere at increasing Wi. These low-pressure regions exist near the rear stagnation points and represent the roots of the viscoelastic wings on the sphere surface. As described in Sec. IV, we have examined the drag components (from pressure or form drag, viscous drag, and polymeric drag contributions) on the sphere, considering both the total drag (Sec. IV A) and later isolating the coupling drag (Sec. IV B). For all parameter regimes where $\Theta_0 \sim O(1)$, the form drag is the dominant contribution to the total and coupling drag.

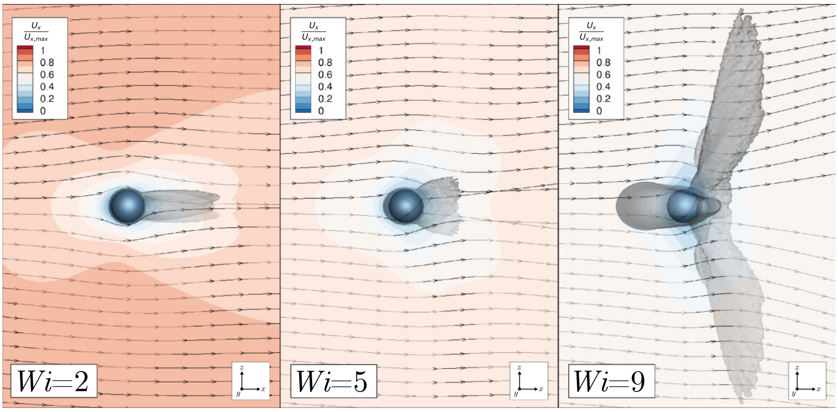

FIG. 19. Contour plots of $U_x/U_{x,\max}$ (at 40% translucency) at $y = 0$ and on the surface of the sphere, viewed from the y direction, for $\Theta_0 = 4.65$ and $\epsilon = 0.48$. Semitranslucent isosurface plots of the trace of the conformation tensor at 30% of maximum extensibility are shown. Streamlines of (U_x, U_y, U_z) are shown and were seeded at the inlet of the computational domain at $y = 0$.

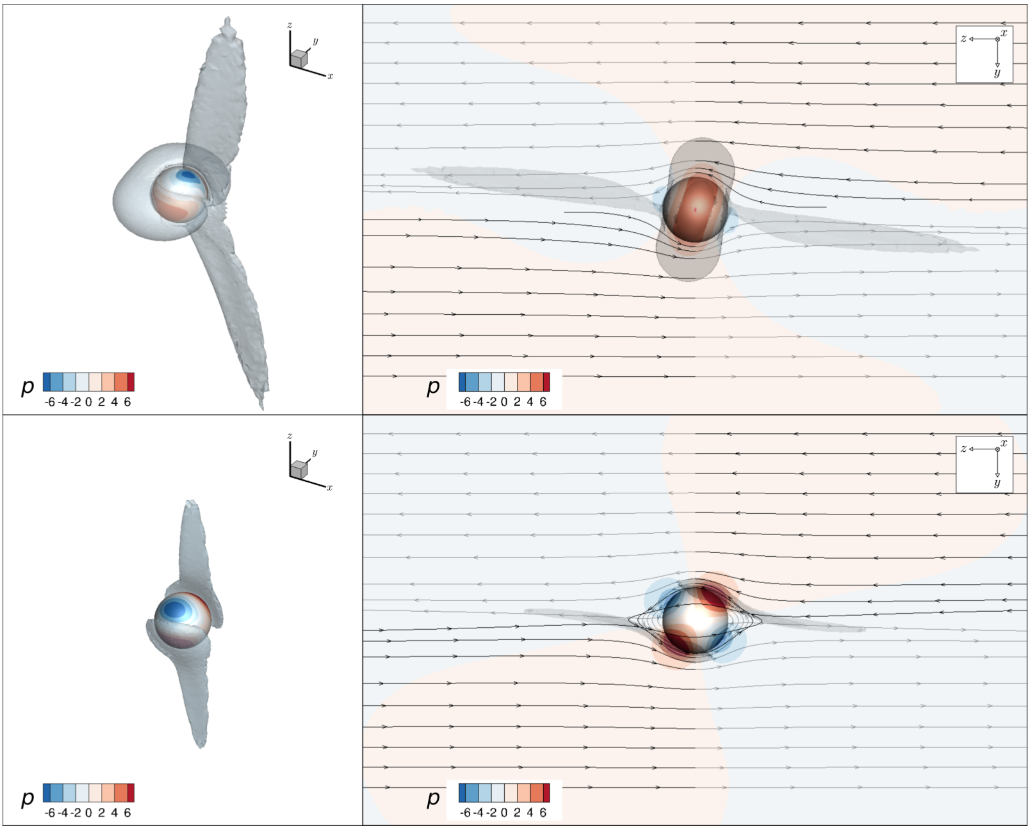

FIG. 20. Comparison of the viscoelastic wake structures that form for a sphere ($\epsilon = 0.16$) settling in BF1 with $\Theta_0 = 2.09$ (top) vs in fluid BF2 with $\Theta_0 = 0.14$ (bottom) at $\mathrm{Wi} = 5$. The sphere is settling into the $-x$ direction and is viewed from two different angles (left and right). Contours of pressure [minus the hydrostatic pressure and made dimensionless with U_{sed} ($\mathrm{Wi} = 0$) η_0/a] are shown on the surface of the sphere, as well as in a slice with 40% translucency at $x = 0$ (right). Streamlines are seeded at $x = z = 0$ across a range of y. Semitranslucent isosurfaces of the trace of the polymer conformation tensor are shown at 40% of the maximum trace.

The viscoelastic wake structures that develop around the sphere and modify the flow are not limited to the winglike portions that extend into the shear direction. From Fig. 16 it is evident that these structures grow around the sphere surface in the sedimentation and gradient directions, in addition to the shear direction, at high Wi. These regions likely also contribute to the deflection of fluid flow and consequently to the increase in pressure drag on the sphere. In Fig. 18, we see that the high-pressure region that develops on the front side of the sphere is locally correlated with the region of high polymer stretch that develops around the sphere at high Wi. In Fig. 19, we show that streamlines originating at the stagnation line at the inlet of the computational domain at $y = 0$ are deflected around a region containing the sphere and an extended region of high polymer stretching. This is seen from the streamlines and the contour plots of velocity, which show that the x direction velocity disturbance extends well into the shear direction (which was also seen in Fig. 16).

In this section, we showed that at $O(1)$ values of Θ_0 and high Wi, regions of high polymer stretch and tension extend into three dimensions, deflecting streamlines, and ultimately retarding motion of the sphere. The decrease in particle mobility from orthogonal shear is primarily due to the increase in the form drag, although the viscous drag also increases with the same scaling, as shown in Fig. 10. In essence, the effective body in motion, at high Weissenberg number, becomes the rigid sphere plus an extended region of stretched polymer.

C. Comparison to weakly elastic fluids

In Fig. 20, we compare visualizations of a sphere settling in BF1 at $\Theta_0 = 2.09$ (top) and a sphere settling in BF2 at $\Theta_0 = 0.14$ (bottom) for $\epsilon = 0.16$ and $\mathrm{Wi} = 5$. For the lower Θ_0, more weakly elastic fluid flow, viscoelastic structures do form around the sphere, as in the case of the highly elastic fluid. However, since the flow is dominated by the shear flow rather than the uniform flow past the sphere, these structures grow predominately in the shear direction, like viscoelastic tongues. These structures were observed previously by Padhy *et al.* [33] for shear-dominated flows at $\Theta = 0.1$. Nearly symmetric regions of high and low pressure are observed on the sides of the sphere from the strong viscoelastic shear flow. This is in contrast with the highly elastic fluid case, where a high-pressure region develops on the front side of the sphere. From analysis of the streamlines in the case of the weakly elastic fluid, we see that the fluid that comes close to the sphere surface can rotate with the sphere for several rotations before moving past the sphere. For these flows, the coupling drag can be dominated by the viscous drag at high Wi, as shown previously by Padhy *et al.* [32,33] and in this work.

VI. CONCLUSION

We have examined the mobility of a particle moving in a highly elastic fluid under confined orthogonal shear. We have presented results from experiments and numerical simulations showing a significant decrease in particle mobility at increasing orthogonal shear rates. Using the simulation results, we have observed the formation of viscoelastic wake structures, which develop into viscoelastic wings at high shear Weissenberg number and $O(1)$ values of the sedimentation Weissenberg number. We have proposed that the form drag created by these viscoelastic wake structures in orthogonal shear accounts for decreasing particle mobility when the fluid is highly elastic, i.e., when the polymer deformation created by the motion associated with the applied force on the particle is significant. Because these regions of high polymer tension act to deflect streamlines and enhance drag, the effective body in motion becomes the particle plus an extended region of stretched polymer. This result has broad implications for applications involving the movement of particles in deformed viscoelastic fluids and suggests a method for enhanced control of particle mobility, namely, through the modification of the wake structures, by tuning the particle shape and size, the elastic fluid properties, and the fluid deformation.

ACKNOWLEDGMENTS

This material is based upon work supported by the National Science Foundation under Grants No. DGE-114747 (W.L.M.) and No. CBET-1337051, the Stanford Natural Gas Initiative, the U.S. Army High Performance Computing Research Center (AHPCRC), and the Stanford Certainty computer cluster, which is funded by the American Recovery and Reinvestment Act Grant No. W911NF07200271. Part of this work was performed at the Stanford Nano Shared Facilities, supported by the National Science Foundation under Award No. ECCS-1542152. The authors would like to thank Leon Cox for his contributions to the experiments.

W.L.M. and S.K. contributed equally to this work.

---

[1] J. Ashwin and A. Sen, Microscopic Origin of Shear Relaxation in a Model Viscoelastic Liquid, Phys. Rev. Lett. **114**, 055002 (2015).

[2] A. M. Leshansky, A. Bransky, N. Korin, and U. Dinnar, Tunable Nonlinear Viscoelastic "Focusing" in a Microfluidic Device, Phys. Rev. Lett. **98**, 234501 (2007).

[3] A. C. Barbati, J. Descroches, A. Robisson, and G. H. McKinley, Complex fluids and hydraulic fracturing, Annu. Rev. Chem. Biomol. Eng. **7**, 415 (2016).

[4] G. G. Stokes, On the effect of the internal friction of fluids on the motion of pendulums, Trans. Cambr. Philos. Soc. **9**, 8 (1850).

[5] R. B. Bird, R. C. Armstrong, and O. Hassager, *Dynamics of Polymeric Liquids, Volume 1: Fluid Mechanics*, 2nd ed. (Wiley-Interscience, New York, 1987).

[6] R. B. Bird, C. F. Curtiss, R. C. Armstrong, and O. Hassager, *Dynamics of Polymeric Liquids, Volume 2: Kinetic Theory*, 2nd ed. (Wiley-Interscience, New York, 1987).

[7] D. V. Boger, A highly elastic constant-viscosity fluid, J. Non-Newton. Fluid Mech. **3**, 87 (1977).

[8] G. H. McKinley, D. DeKee, and R. P. Chhabra, *Transport Processes in Bubbles, Drops and Particles*, 2nd ed. (CRC, Boca Raton, 2002), Chap. 14.

[9] B. Caswell, O. Manero, and B. Mena, Recent developments on the slow viscoelastic flow past spheres and bubbles, Rheol. Rev. **2004**, 197 (2004).

[10] R. P. Chhabra, *Bubbles, Drops, and Particles in Non-Newtonian Fluids*, 2nd ed. (CRC, Boca Raton, 2007).

[11] M. D. Chilcott and J. M. Rallison, Creeping flow of dilute polymer solutions past cylinders and spheres, J. Non-Newton. Fluid Mech. **29**, 381 (1988).

[12] O. G. Harlen, High-Deborah-number flows of dilute polymer solutions, J. Non-Newton. Fluid Mech. **37**, 157 (1990).

[13] M. T. Arigo, D. Rajagopalan, N. Shapley, and G. H. McKinley, The sedimentation of a sphere through an elastic fluid. Part 1. Steady motion, J. Non-Newton. Fluid Mech. **60**, 225 (1995).

[14] F. Snijkers, G. D'Avino, P. L. Maffettone, F. Greco, M. A. Hulsen, and J. Vermant, Rotation of a sphere in a viscoelastic liquid subjected to shear flow. Part II. Experimental results, J. Rheol. **53**, 459 (2009).

[15] K. D. Housiadas and R. I. Tanner, Perturbation solution for the viscoelastic 3D flow around a rigid sphere subject to simple shear, Phys. Fluids **23**, 083101 (2011).

[16] G. D'Avino, M. A. Hulsen, F. Snijkers, J. Vermant, F. Greco, and P. L. Maffettone, Rotation of a sphere in a viscoelastic liquid subjected to shear flow. Part I: Simulation results, J. Rheol. **52**, 1331 (2008).

[17] F. Snijkers, G. D'Avino, P. L. Maffettone, F. Greco, M. A. Hulsen, and J. Vermant, Effect of viscoelasticity on the rotation of a sphere in shear flow, J. Non-Newton. Fluid Mech. **166**, 363 (2011).

[18] H. Faxén, Der Widerstand gegen die Bewegung einer starren Kugel In einer zähen Flüssigkeit, die zwischen zwei parallelen ebenen Wänden eingeschlossen ist, Ann. Phys. **373**, 89 (1922).

[19] A. J. Goldman, R. G. Cox, and H. Brenner, Slow viscous motion of a sphere parallel to a plane wall – I Motion through a quiescent fluid, Chem. Eng. Sci. **22**, 637 (1967).

[20] B. P. Ho and L. G. Leal, Inertial migration of rigid spheres in two-dimensional unidirectional flows, J. Fluid Mech. **65**, 365 (1974).

[21] P. Ganatos, S. Weinbaum, and R. Pfeffer, A strong interaction theory for the creeping motion of a sphere between plane parallel boundaries. Part 2. Parallel motion, J. Fluid Mech. **99**, 755 (1980).

[22] A. Miyamura, S. Iwasaki, and T. Ishii, Experimental wall correction factors of single solid spheres in triangular and square cylinders, and parallel plates, Int. J. Multiphase Flow **7**, 41 (1981).

[23] B. H. A. A. van den Brule and G. Gheissary, Effects of fluid elasticity on the static and dynamic settling of a spherical particle, J. Non-Newton. Fluid Mech. **49**, 123 (1993).

[24] K. D. Housiadas and R. I. Tanner, The drag of a freely sedimentating sphere in a sheared weakly viscoelastic fluid, J. Non-Newton. Fluid Mech. **183–184**, 52 (2012).

[25] K. D. Housiadas, Stress diffusion and high order viscoelastic effects in the 3D flow past a sedimenting sphere subject to orthogonal shear, Rheol. Acta **53**, 537 (2014).

[26] K. D. Housiadas and R. I. Tanner, Rheological effects in the 3D creeping flow past a sedimenting sphere subject to orthogonal shear, Phys. Fluids **26**, 013102 (2014).

[27] R. I. Tanner, K. D. Housiadas, and F. Qi, Mechanism of drag increase on spheres in viscoelastic cross-shear flows, J. Non-Newton. Fluid Mech. **203**, 51 (2014).

[28] J. Einarsson and B. Mehlig, Spherical particle sedimenting in weakly viscoelastic shear flow, Phys. Rev. Fluids **2**, 063301 (2017).

[29] N. Tonmukayakul, J. F. Morris, and R. Prud'homme, Method for estimating proppant transport and suspendability of viscoelastic liquids, U.S. Patent No. 8,424,368 (23 April 2013).

[30] G. Gheissary and B. H. A. A. van den Brule, Unexpected phenomena observed in particle settling in non-Newtonian media, J. Non-Newton. Fluid Mech. **67**, 1 (1996).

[31] Y. T. Hu, H. Chung, and J. E. Maxey, *SPE Hydraulic Fracturing Technology Conference*, SPE-173339-MS (Society of Petroleum Engineers, Richardson, 2015) .

[32] S. Padhy, E. S. G. Shaqfeh, G. Iaccarino, J. F. Morris, and N. Tonmukayakul, Simulations of a sphere sedimenting in a viscoelastic fluid with cross shear flow, J. Non-Newton. Fluid Mech. **197**, 48 (2013).

[33] S. Padhy, M. Rodriguez, E. S. G. Shaqfeh, G. Iaccarino, J. F. Morris, and N. Tonmukayakul, The effect of shear thinning and walls on the sedimentation of a sphere in an elastic fluid under orthogonal shear, J. Non-Newton. Fluid Mech. **201**, 120 (2013).

[34] B. Yang and B. Khomami, Simulations of sedimentation of a sphere in a viscoelastic fluid using molecular based constitutive models, J. Non-Newton. Fluid Mech. **82**, 429 (1999).

[35] A. Abedijaberi and B. Khomami, Sedimentation of a sphere in a viscoelastic fluid: A multiscale simulation approach, J. Fluid Mech. **694**, 78 (2012).

[36] I. E. Garduñ, H. R. Tamaddon-Jahromi, and M. F. Webster, The falling sphere problem and capturing enhanced drag with Boger fluids, J. Non-Newton. Fluid Mech. **231**, 26 (2016).

[37] H. Yatou, Flow pattern transition accompanied with sudden growth of flow resistance in two-dimensional curvilinear viscoelastic flows, Phys. Rev. E **82**, 036310 (2010).

[38] D. Richter, G. Iaccarino, and E. S. G. Shaqfeh, Simulations of three-dimensional viscoelastic flows past a circular cylinder at moderate Reynolds numbers, J. Fluid Mech. **651**, 415 (2010).

[39] M. Yang, S. Krishnan, and E. S. G. Shaqfeh, Numerical simulations of the rheology of suspensions of rigid spheres at low volume fraction in a viscoelastic fluid under shear, J. Non-Newton. Fluid Mech. **234**, 51 (2016).

[40] D. V. Boger and H. Nguyen, A model viscoelastic fluid, Polym. Eng. Sci. **18**, 1037 (1978).

[41] D. F. James, Boger fluids, Annu. Rev. Fluid Mech. **41**, 129 (2009).

[42] G. D'Avino, F. Snijkers, R. Pasquino, M. A. Hulsen, F. Greco, P. L. Maffettone, and J. Vermant, Migration of a sphere suspended in viscoelastic liquids in Couette flow: Experiments and simulations, Rheol. Acta **51**, 215 (2012).

[43] G. D'Avino, F. Greco, and P. L. Maffettone, Particle migration due to viscoelasticity of the suspending liquid and its relevance in microfluidic devices, Annu. Rev. Fluid Mech. **49**, 341 (2017).

[44] G. D'Avino, G. Cicalea, M. A. Hulsen, F. Greco, and P. L. Maffettone, Effects of confinement on the motion of a single sphere in a sheared viscoelastic liquid, J. Non-Newton. Fluid Mech. **157**, 101 (2009).

[45] M. J. Solomon and S. J. Muller, Flow past a sphere in polystyrene-based Boger fluids: The effect on the drag coefficient of finite extensibility, solvent quality and polymer molecular weight, J. Non-Newton. Fluid Mech. **62**, 81 (1996).